AN ABSTRACT OF THE THESIS OF

Bryan A. Maack for the degree of Master of Science in Materials Science presented on November 12, 2015.

Title: Developing New Routes for Mechanical Characterization of Metal-Organic Frameworks

Abstract approved:

_____

Brady J. Gibbons

Metal-organic frameworks (MOFs) represent an exciting, new class of porous materials. Their hybrid organic-inorganic structure opens up near infinite possibilities to tune and design their structure for specific properties and applications. A new generation of flexible MOFs, following a generation of stiff MOFs, has created additional design space and complexity. To date, the properties even of known MOFs, especially mechanical properties, remain largely unexplored. In this thesis, methods to synthesize MOFs and characterize their mechanical properties are explored.

Solvothermal methods were chosen to synthesize MOF-5, a stiff MOF, and MIL-53(Al), a flexible MOF. X-ray diffraction data proved that both MOFs were synthesized in phase pure form. Immobilization and polishing methods were developed to prepare the MOFs for mechanical testing. S1813 photoresist and Buehler epoxy were chosen as media to immobilize MIL-53(Al). The goal was to produce samples flat enough for reproducible and consistent mechanical measurements using nanoindentation and atomic force microscopy.

Mechanical testing produced high quality, reproducible measurements. However, the media employed to immobilize the MOFs, as well as the polishing process, played an undesired role in altering both the structure and mechanical properties of the MOFs. AMFM, an AFM mode capable of mapping mechanical properties, produced images of MIL-53(Al) immobilized in S1813 photoresist showing elastic moduli of 7 to 7.5 GPa for the MIL-53(Al) particles. AMFM of MIL-53(Al) immobilized in Buehler epoxy produced images of MIL-53(Al) with elastic moduli from 8 to 12 GPa. Nanoindentation proved inconclusive for determining the elastic modulus of MIL-53(Al) in S1813 since the system was not sensitive enough to reliably indent small MIL-53(Al) particles that ranged in size from 1 to 5 μm.

©Copyright by Bryan A. Maack
November 12, 2015
All Rights Reserved

Developing New Routes for Mechanical Characterization of Metal-Organic Frameworks

by
Bryan A. Maack

A THESIS

submitted to

Oregon State University

in partial fulfillment of
the requirements for the
degree of

Master of Science

Presented November 12, 2015
Commencement June 2016

Master of Science thesis of Bryan A. Maack presented on November 12, 2015.

APPROVED:

Major Professor, representing Materials Science

Director of the Materials Science Program

Dean of the Graduate School

I understand that my thesis will become part of the permanent collection of Oregon State University libraries. My signature below authorizes release of my thesis to any reader upon request.

Bryan A. Maack, Author

ACKNOWLEDGEMENTS

Dr. Gibbons put up with me for *6 years*. And I wasn't even getting a PhD. That fact, more than anything else, testifies to his quality of character. I came to him a young freshman—loud, obnoxious, and generally socially unacceptable—and he helped me become the kind of person you can at least take outside the lab and (possibly) trust with a master's degree. But seriously, Brady is a great guy. He's bright and funny, dedicated to his students and good work. He's patient with us, questionable lot that we are, and guides with a kind yet firm hand. This man has in no small part set the course of my life. I will miss Brady.

Ashley Mason has had the (mis)fortune of knowing me for 4 years. She's witty and sarcastic but we all know she has a heart of gold. You just have to dig down past the amusing comments and Diet Dr. Pepper, but I promise it's there. She also has the (mis)fortune of being the only person capable of taking readable meeting minutes, kind of like how mom made your sister empty the dishwasher if you did it badly enough. But really, Ashley is awesome. She provides moral support when we're super-duper frustrated, and her electrical engineering background is very useful, especially to chemical engineers like me who still struggle even to plug in machines. She proofreads our papers (did I mention she's the only person who can write?) and makes us laugh. I will miss Ashley greatly.

Austin Fox(y) has only needed to deal with me for 3 years, a relatively short time but still more than enough for one lifetime. His mechanical capability is unsurpassed. I'm not sure how the lab would still be running without him. He's got a good sense of humor and was always willing to let me watch him fix stuff while kindly explaining the process,

because I can't plug in machines let alone fix them. He also did the SEM for this project, saving me a great amount of trouble. Thanks dude! I would miss him, but he's probably going to end up in Portland at some point anyways because he's got a beard, plays bike polo, and likes organic food.

Joel Walenza-Slabe (or however you spell his last name) comes in second place having dealt with me for 5 years. However, Joel is probably the only member of the group weirder than me, so I think it goes both ways. Really, though, he's a great guy with a big heart. He takes all of our sarcastic comments and laughs along with us, although that might be because he wasn't paying attention anyways. He works hard and diligently. He showed me how to polish samples effectively, saving me a great amount of trouble on a process that is already very much trial-and-error frustration. I guess I'll miss Joel. He's kinda weird and smelly, though.

Dr. Alex Greaney has served as an excellent team leader on this project. He came up with ideas on how to keep the project moving, and he also has a good sense of humor. I hear there are funny pictures of him when he was a cox for the Oxford rowing team. But you didn't hear that from me.

I thank Dr. Greg Herman and Dr. Frank Tepley for agreeing to be a committee member and GRC, respectively. I obviously would not have a chance to graduate without them.

I thank the Keck Foundation for providing the funding for this project.

Last, but certainly not least, my beloved Taya. She has been the person keeping me going. Her kind heart and kind (but firm!) words kept me moving forward when,

quite frankly, I was out of gas. I love her. And by the time this thesis is (hopefully) published, we'll be married. Wahoo!

TABLE OF CONTENTS

Page

Chapter 1: Introduction 1
1.1 Project Objectives 1
Chapter 2: Background 3
2.1 Metal-Organic Frameworks 3
2.2 Properties of Metal-Organic Frameworks 5
2.3 Synthesis and Design of Metal-Organic Frameworks 6
2.4 MOF-5 7
2.5 Flexible MOFs 8
2.6 MIL-53 10
2.7 Mechanical Properties of Metal-Organic Frameworks 11
2.8 Nanoindentation 14
2.9 Mechanical Properties of MOF-5 18
2.10 Mechanical Properties of MIL-53 19
2.11 Atomic Force Microscopy 20
2.12 Amplitude Modulation – Frequency Modulation (AMFM) 23
Chapter 3: Experimental 28
3.1 Synthesis of MOF-5 28
3.2 Synthesis of MIL-53(Al) 28
3.3 Immobilizing MIL-53(Al) 28
3.4 Optical Microscopy 30
3.5 X-ray diffraction 30
3.6 AFM and AMFM 30
3.7 Nanoindentation 30
3.8 SEM 31
3.9 Thermogravimetric Analysis 31
3.10 PowderCell 2.4 31
Chapter 4: Results and Discussion 32

TABLE OF CONTENTS (Continued)

Page

4.1 Synthesis of MOF-5 32
4.2 Synthesis of MIL-53(Al) 34
4.3 Immobilization of MIL-53(Al) 43
4.4 Nanoindentation of MIL-53(Al) in S1813 48
4.5 AMFM of MIL-53(Al) in S1813 55
4.6 MIL-53(Al) in Buehler Epoxy 58
4.7 AMFM of MIL-53(Al) in Buehler Epoxy 62
Chapter 5: Conclusions and Future Work 66
5.1 Synthesis of MOFs 66
5.2 Immobilization of MOFs 66
5.3 Mechanical Characterization of MOFs 67
5.4 Future Work 68

LIST OF FIGURES

Figure Page

Figure 2.1: Comparing MOFs to polymers and zeolites. 3
Figure 2.2: MOFs came out of research into coordination polymers. 4
Figure 2.3: MOFs can be separated into three generations. 4
Figure 2.4: MOF-5 consists of zinc nodes connected by benzenedicarboxylate linkers. ... 8
Figure 2.5: The structure of flexible MOFs respond to pressure in a number of ways..... 9
Figure 2.6: MIL-53(Al) can assume three forms. 10
Figure 2.7: Metal node choice plays a role in the flexibility of MIL-53. 11
Figure 2.8: Loading of MOFs under pressure. 12
Figure 2.9: Hardness versus elastic modulus for porous materials. 13
Figure 2.10: A Berkovich tip is a three-sided pyramid. 14
Figure 2.11: Example of load-displacement curve. 15
Figure 2.12: The surface profiles of interest for nanoindentation. 16
Figure 2.13: (a) The structure of MOF-5 is overlaid with directional axes. (b) Plotting elastic modulus as a function of orientation. 19
Figure 2.14: MIL-53(Al)-lp displays highly anisotropic elastic moduli. 19
Figure 2.15: AFM provides a wide range of scanning capability. 20
Figure 2.16: The AFM cantilever. 20
Figure 2.17: Laser, cantileer, and detector for AFM. 21
Figure 2.18: Explanation of photodiode in AFM. 21
Figure 2.19: Piezoelectric elements of an AFM. 22
Figure 2.20: The first four vibrational modes of a typical cantilever. 23
Figure 2.21: Excitation forces excite the cantilever at its two resonances. 24
Figure 2.22:.The first and second resonance in AMFM. 26
Figure 2.22: Example AMFM images. 27
Figure 4.1: Insufficient washing of MOF-5 with DMF. 32
Figure 4.2: The diffraction pattern of phase-pure MOF-5 from Panella *et al.* 33
Figure 4.3:. This diffraction pattern of MOF-5 at 6 hours after synthesis. 33
Figure 4.4: MIL-53(Al)-as diffraction pattern. 34
Figure 4.5: The diffraction pattern of MIL-53(Al)-as from the work of Loiseau *et al.* 35

LIST OF FIGURES (Continued)

Figure Page

Figure 4.6: MIL-53(Al)-lt diffraction pattern. 35
Figure 4.7: The diffraction pattern of MIL-53(Al)-lt from the work of Loiseau *et al.* 36
Figure 4.8: Attempting to synthesize MIL-53(Al) in a 45 mL pressure vessel. 37
Figure 4.9: PowderCell generated and indexed pattern for MIL-53(Al)-as. 38
Figure 4.10: PowderCell generated and indexed pattern for MIL-53(Al)-lt. 38
Figure 4.11: Extraneous peaks in some batches of MIL-53(Al)-lt. 40
Figure 4.12: TGA on MIL-53(Al)-lt. 41
Figure 4.13: TGA on MIL-53(Al)-lt from Loiseau *et al.* 41
Figure 4.14: A large area SEM scan on MIL-53(Al)-lt 42
Figure 4.15: Smaller area scan of MIL-53(Al)-lt. 42
Figure 4.16: 5x magnification optical micrograph of MIL-53(Al) particles in S1813 before polishing the sample. 43
Figure 4.17: Immobilizing MIL-53 in S1813 resulted in peak shifts. 44
Figure 4.18: 50x magnification micrograph of MIL-53 in S1813 after polishing. 45
Figure 4.19: SEM imaging of polished MIL-53(Al) particles in S1813. 46
Figure 4.20: Magnified SEM image of MIL-53(Al) particles in S1813. 46
Figure 4.21: Magnified SEM image of MIL-53(Al) particles in S1813. 46
Figure 4.22: Comparison of diffraction patterns 47
Figure 4.23: Indentation of S1813 photoresist. 48
Figure 4.24: Load-diplsacement curves from indenting S1813 48
Figure 4.25: Histogram of elastic moduli from S1813. 49
Figure 4.26: Plotting elastic moduli of S1813 49
Figure 4.27: Point map of measured elastic moduli for S1813. 50
Figure 4.28: Indenting MIL-53(Al) in S1813. 51
Figure 4.29: The load-displacement curves of MIL-53(Al) in S1813 51
Figure 4.30: Histogram compiling the elastic moduli calculated for MIL-53(Al) in S1813. 52
Figure 4.31: Map plotting the elastic modulus calculated from each point of the indentation experiment. 52

LIST OF FIGURES (Continued)

Figure Page

Figure 4.34: Plot showing the load-displacement measurements from the 1 mN indentations of MIL-53(Al) in S1813. 53

Figure 4.35: Plot showing the load-displacement measurements from the 0.5 mN indentations of MIL-53(Al) in S1813. 53

Figure 4.36: Histogram comparing the calculated elastic moduli from the 2 mN, 1 mN, and 0.5 mN indentation experiments. 54

Figure 4.37: Histogram combining the elastic moduli calculated from the 1 mN and 0.5 mN indentations. 55

Figure 4.38: AMFM Scan area with large concentration of MIL-53(Al) particles..... 56

Figure 4.39: AMFM Scan area with a low concentration of MIL-53(Al) particles..... 57

Figure 4.40: 5x optical micrograph of MIL-53(Al) in Buehler epoxy before polishing... 58

Figure 4.41: Comparison of diffraction patterns for MIL-53(Al) in epoxy 59

Figure 4.42: 20x optical micrograph of MIL-53(Al) in Buehler epoxy after polishing.... 60

Figure 4.43: 50x optical micrograph of MIL-53(Al) in Buehler epoxy after polishing.... 60

Figure 4.44: Comparison of diffraction patterns for MIL-53(Al) in epoxy after polish... 61

Figure 4.45: AMFM scan area with higher concentration of MIL-53(Al). 63

Figure 4.46: AMFM scan area with lower concentration of MIL-53(Al)..... 64

Chapter 1: Introduction

Metal-Organic Frameworks (MOFs) represent a relatively young area of study in materials science. MOFs consist of both organic and inorganic components. Previously, porous solids were either purely inorganic, like zeolites, or purely organic, like activated carbon. The combination of organic and inorganic components opens up new opportunities to achieve superior properties and, more interestingly, design porous solids with particular properties and applications in mind. Furthermore, a new generation of flexible MOFs has arisen, where traditional MOFs have been rigid. These flexible MOFs present a new opportunity to study MOFs that have been characterized very little even by the standards of this young field.

The mechanical properties of MOFs in particular remain largely unexplored. Nanoindentation has been a common method for measuring mechanical properties. The Oliver-Pharr method is used to analyze the load-displacement curves from nanoindentation and calculate elastic modulus. Another method, atomic force microscopy (AFM), now possesses the ability to map the mechanical properties of a material surface. The sensitivity of the AFM is able to detect differences in mechanical properties on a scale smaller than nanoindentation. This thesis will combine both methods to characterize the mechanical properties of MOFs in order to better understand and design MOFs.

1.1 Project Objectives

This project seeks to establish synthesis routes for MOFs and characterize the mechanical properties of these MOFs. Specific goals include:

1) Establishing synthesis routes of MOFs for future use by the Multi-functional Thin Film Materials Group at Oregon State University.

2) Establishing preparation methods of MOFs for characterization.
3) Characterizing the structure and mechanical properties of the synthesized MOFs.

Chapter 2: Background

2.1 Metal-Organic Frameworks

MOFs consist of metal atoms or groups of metal atoms connected by organic ligands. This hybrid organic-inorganic structure contains a central pore whose volume is defined by the length of the organic ligands. The metal atom groups are commonly referred to as nodes and the organic ligands as linkers. MOFs represent a new class of hybrid porous materials where porous solids, until the 1990s, consisted largely of either purely inorganic components, like zeolites, or carbon-based and thus organic components, like activated carbon [1].

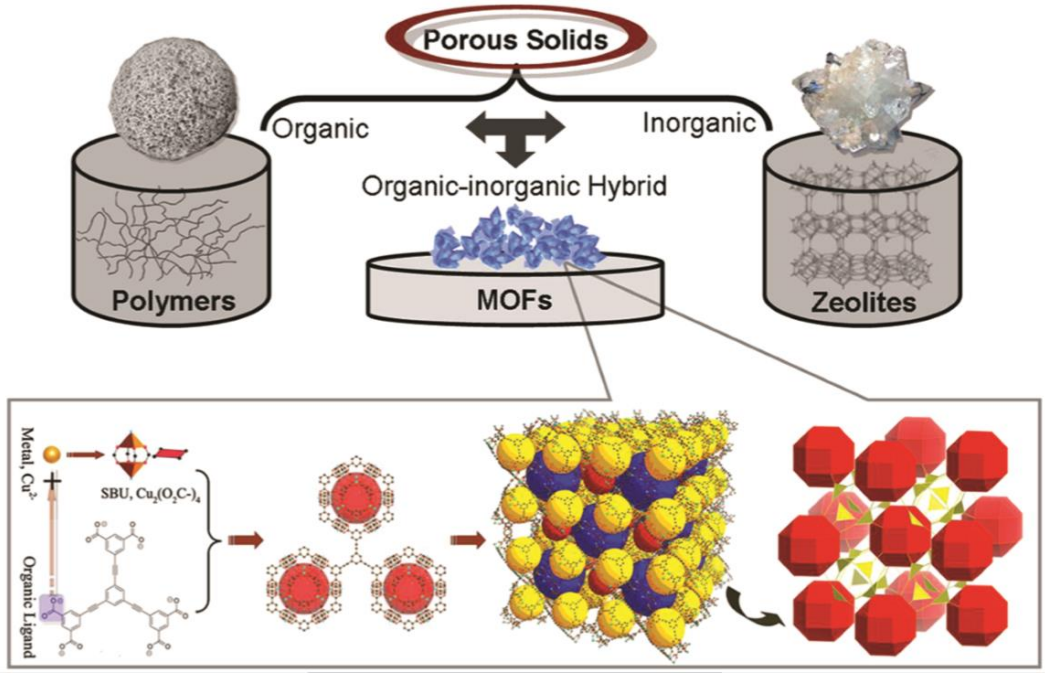

Figure 2.1: Polymers are shown on the top left as an example of organic porous solids while zeolite are shown on the top right as an example of inorganic porous solids. MOFs combine organic and inorganic components to form a hybrid organic-inorganic porous structure. The bottom shows the general procedure for building a MOF, starting from metal nodes and organics linkers and building up to a complete crystalline structure [1].

Coordination polymers in general date back to the 1960s, but particular interest in MOFs began in the early 1990s and has accelerated greatly since 2005 as seen in Figure 2.2.

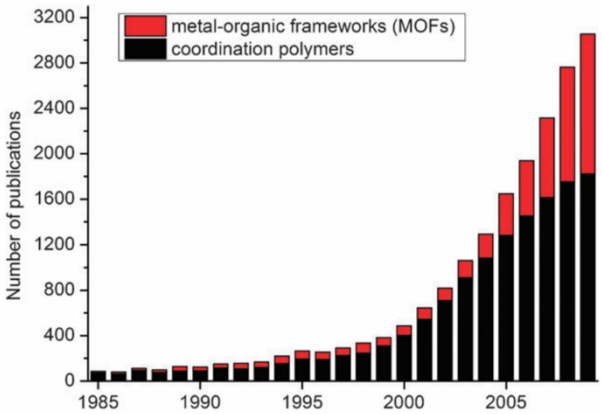

Figure 2.2: MOFs came out of research into coordination polymers. MOF publications have grown tremendously since the 1990s [2].

Researchers separate MOFs into three generations. First generation MOFs lack permanent porosity because they collapse once guest molecules inside the pores are removed. Second generation MOFs consist of stable structures that remain porous through absorption or desorption of guest molecules. Third generation MOFs consist of flexible MOFs that change shape in response to external stimuli such as pressure and temperature [3]. The stimuli cause either expansion or contraction, based on the structure of the MOF, with displacements exceeding 10 Å [4]. Figure 2.3 illustrates the three generations of MOFs.

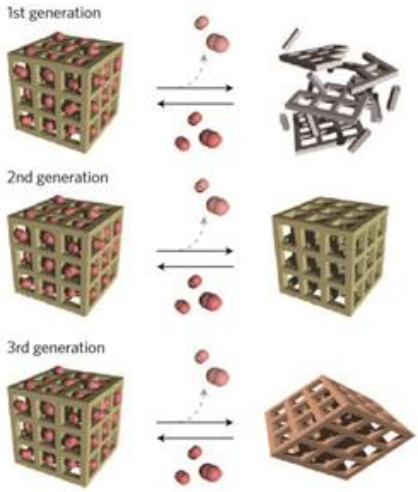

Figure 2.3: MOFs can be separated into three generations: MOFs that lose porosity upon guest removal, MOFs that retain porosity upon guest absorption or removal, and MOFs that change shape in response to external stimuli such as guest absorption or desorption [3].

Researchers designate MOFs using a wide array of three letter identifiers. Some titles refer to the structure of the MOF, e.g. ZIF (zeolitic imidazolate framework) refers to MOFs that structurally resemble zeolites, and IRMOF (isoreticular MOF) refers to a series of MOFs that share the same node with slightly different linkers. Other titles refer to the laboratory from which the MOF originated, e.g. MIL (Materials Institute Lavoisier) and HKUST (Hong Kong University of Science and Technology [1].

2.2 Properties of Metal-Organic Frameworks

Interest in MOFs comes from their highly tunable properties and the wide variety of potential applications that these properties enable. MOFs can absorb and store significant quantities of gases such as hydrogen, carbon dioxide, carbon monoxide, methane, and oxygen for purposes ranging from energy storage to pollution reduction [4]. Controllable pore size allows MOFs to serve as catalysts with customizable selectivity [2]. Other applications include ion exchange, drug delivery, chemical sensing, and radiation sensing [5]. Large pore MOFs, with openings in the range of 20 to 500 Å, perform well as catalysts. Small pore MOFs, with openings smaller than 20 Å, are best for gas storage and separation due to the strong interaction between gas molecules and pore walls [6].

MOFs possess a number of advantages over competing materials like zeolites and activated carbon. MOFs have higher surface area per unit weight than zeolites and activated carbon, allowing more active sites for catalysis and pores for gas absorption [1]. Unlike purely inorganic structures, MOFs can use almost all cations. This variety, combined with numerous organic linkers, leads to an extensive array of options for constructing MOFs [4]. The ordered structure of MOFs, which activated carbon lacks,

allows for clear phase identification with x-ray diffraction [6-7]. Lastly, the solvent used during MOF synthesis acts as the template. Normally, purely inorganic structures require an additional component beyond the solvent that guides the reaction to produce the desired structure [4].

MOFs also present some unique challenges. The same variety that gives MOFs their vast potential creates the challenge of identifying useful MOFs among the seemingly limitless theoretical MOFs [4]. The larger the MOF pore, the higher likelihood of collapse upon removing any solvent molecules from the pore [6]. MOFs possess weak thermal stability in the range of 350-400 °C and seldom more than 500 °C [4]. MOFs are insoluble, excluding typical methods of purification such as distillation [6]. MOFs are difficult to obtain in pure form upon synthesis, compounding the inability to employ traditional purification methods. Tuning of reaction conditions and manually separating desired MOFs can mitigate this disadvantage, but these methods are highly time intensive and do not scale up well beyond 1 gram [7-8].

2.3 Synthesis and Design of Metal-Organic Frameworks

Synthesis of a MOF requires sources for the metal nodes and organic linkers combined with a solvent to contain and template the reaction. Both the chosen metal and organic linker greatly affect the resulting MOF. The linker's bond angle, length, size, and chirality influence the final structure of the MOF [6]. The metal ions will also prefer to adopt certain geometries based on their coordination number. For example, Zn^{2+} can be tetrahedrally, pentahedrally, or octahedrally coordinated while Ni^{2+} is generally octahedral in the presence of oxygen but can be square planar with nitrogen [9].

Synthesis conditions play an extremely important role in MOF formation. Even MOFs with the same designation can have greatly differing properties dependent on synthesis conditions [2]. Temperature, time, solvent choice, concentration of metals and ligands, solubility of the reactants in the solvent, and solution pH all affect the synthesis process. Synthesis temperatures are usually below 300 °C [6]. Synthesis times can range from 3 hours for MOF-5 to 72 hours for MIL-53.

The intentional design of MOF structures has generated both interest and debate in recent years. Completely intentional design seems almost impossible given the near infinite array of possible MOFs. Furthermore, researchers are just beginning to understand the formation mechanisms of MOFs [4]. That being said, a few general rules can guide the synthesis of MOFs. Metals generally adopt certain geometries that can be used to predict the geometry of MOFs made using a particular metal. However, one must consider that a number of metals can adopt multiple geometries. The effects of different solvents must also be considered [1]. One design approach involves taking a known MOF and choosing linkers that are only slightly different from the original linker in order to produce a series of related MOFs [1]. The IRMOFs represent an example of this approach.

2.4 MOF-5

MOF-5 represents one of the earliest MOFs. O.M. Yaghi's research group first synthesized MOF-5 in the late 1990s [10]. MOF-5 consists of zinc metal clusters connected by benzenedicarboxylate (BDC) linkers. The BDC comes from deprotonated terephthalic acid (H_2BDC) which then reacts with Zn^{2+} ions [10]. Zinc clusters are formed from single O atoms bonding with four Zn atoms to form a Zn_4O tetrahedron.

CO_2 groups then connect the edges of the Zn_4O tetrahedron [10]. Figure 2.4 illustrates the structure of MOF-5.

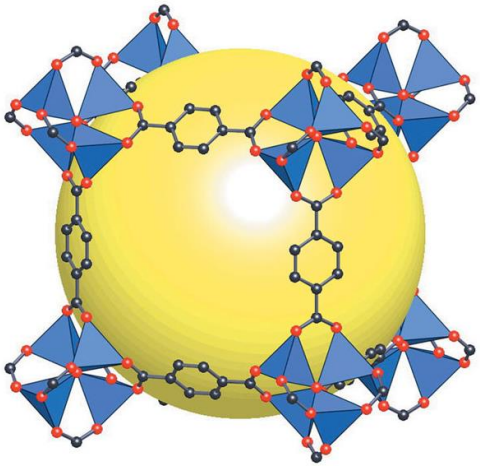

Figure 2.4: MOF-5 consists of $Zn_4O(CO_2)_6$ nodes connected by benzenedicarboxylate linkers. The blue polyhedra are ZnO_4 tetrahedra, while red and black spheres represent oxygen and carbon, respectively. The yellow sphere represents the largest sphere that can fit within the framework [11].

Drying under vacuum or at elevated temperature expels solvent trapped in the pores during synthesis, leaving an enormous amount of pore space in MOF-5. Guest molecules can occupy 55%-61% of the total unit cell volume of 17,295 Å [10]. The crystals remain stable when heated up to 300 °C for 24 hours but exposure to air at room temperature for six weeks will decompose the crystals [10,12].

2.5 Flexible MOFs

Flexible MOFs respond to external stimuli such as temperature, pressure, or guest molecule absorption/desorption, exhibiting structural changes with atomic displacements up to several Å [13]. The MOFs retain their structure through these transformations. In terms of porous solids, MOFs are fairly unique in their ability to possess flexible structures with large displacements [1]. Figure 2.5 gives examples of possible structural changes in flexible MOFs due to mechanical pressure.

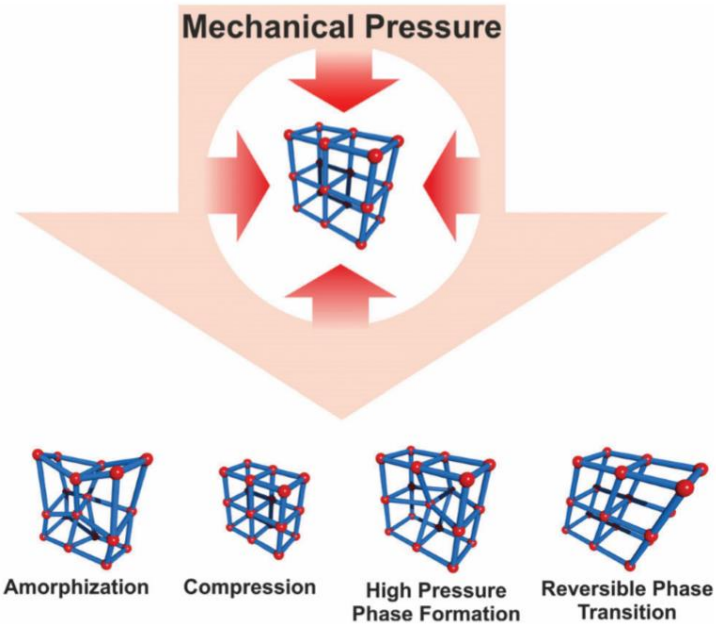

Figure 2.5: The structure of flexible MOFs can respond to pressure in a number of ways [15].

Flexibility in MOFs results from particular structural characteristics. Weak points in the structure, created by weak molecular interactions, in conjunction with strong covalent and coordination bonds allow the MOF to move and exist stably in at least two different structures [13-14]. The MOF must also possess enough open space for the steric hindrances involved with the movement of the flexible portions of the structure [13]. Generally the metal nodes provide rigidity while the organic components provide flexibility, and the ratio of the two will affect the flexibility of the structure [13]. As a result, extremely anisotropic elastic properties result from the structure of these MOFs [15].

Most current applications with flexible MOFs involve sensing and gas separation. High pressures are usually required to purge the as-synthesized flexible structure of any initial guest molecules and thus open the structure for use [13]. One flexible structure, however, opens upon activation with heat--MIL-53.

2.6 MIL-53

MIL-53 is a prototypical and well-studied flexible MOF. MIL-53 actually denotes a family of MOFs that use BDC as the organic linker but employ a number of different metals for the inorganic cluster. These metals include Al, Fe, Cr, Sc, Ga, and In [15]. MIL-53's general structure is $[M(BDC)(OH)]_n$ where M is the metal [15].

As an example, MIL-53 synthesized with aluminum will be discussed because other MIL-53 analogues follow this case closely. MIL-53(Al) has three forms: an as-synthesized form, a high temperature form, and a low temperature form. The as-synthesized form, denoted MIL-53(Al)-as, is $[Al(BDC)(OH)]_n$ with 0.70 molecules of BDC trapped in the pores for every one unit of MIL-53 [16]. The diamond-shaped porous structure is made from corner-sharing $AlO_4(OH)_2$ octahedra connected by BDC linkers and measures 7.3 Å x 7.7 Å in the as-synthesized form [16]. Heating above 275 ºC expels the initial BDC guest molecules, leaving the structure open with 8.5 Å x 8.5 Å pores [16]. This high temperature form is referred to as MIL-53(Al)-ht. Cooling to room temperature causes the structure to reversibly absorb water and shrink to 2.6 Å x 13.6 Å pores as a result of the water absorption, forming the low temperature form denoted MIL-53(Al)-lt [16]. Figure 2.6 illustrates the three forms of MIL-53(Al).

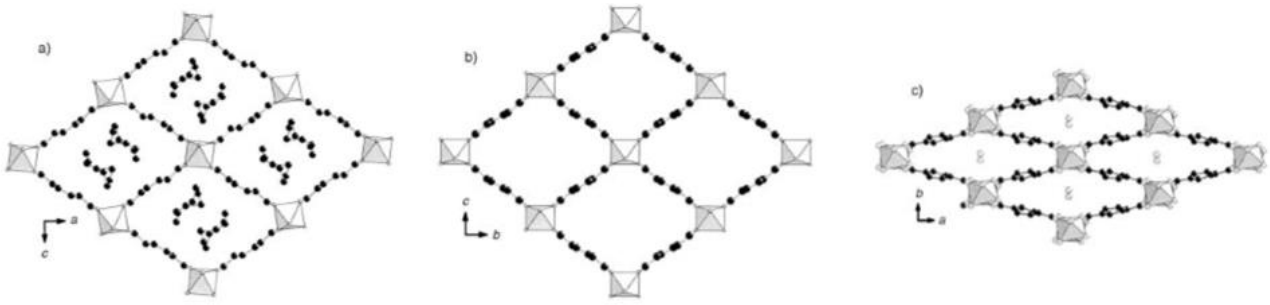

Figure 2.6: MIL-53(Al) can assume three forms: (a) the as-synthesized form, (b) the high temperature form, and (c) the low temperature form. The gray octahedra represent $AlO_4(OH)_2$. The black circles represent carbon. The gray circles represent oxygen [16].

Hydrogen bonding between the water molecules and the carboxylate groups of BDC are responsible for the shrinkage upon absorbing water [16]. The water molecules prefer the oxygen molecules of the carboxylate group [16]. Hydrogen bonding also explains MIL-53's selective absorption of different molecules. MIL-53 will exchange water for dimethylformamide (DMF) due to DMF's strong hydrogen bonding with the structure, but MIL-53 will not exchange water for ethanol or acetone [3].

Synthesizing MIL-53 with different metal nodes affects its properties in many different ways. MIL-53 (Al) has much better thermal stability, up to 500 ºC, than its vanadium or chromium counterparts, which are stable up to 350 ºC [16]. The choice of metal also has a noticeable effect on the flexibility of the structure. Figure 2.7 plots the effect of different metal nodes through the high temperature, low temperature, and as-synthesized forms of MIL-53.

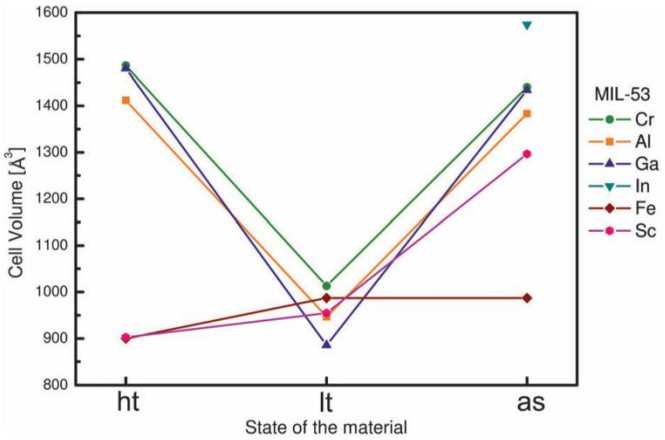

Figure 2.7: Metal node choice plays a role in the flexibility of MIL-53. Most MIL-53 analogues show a contraction in the lt form as water is absorbed into the pores—such as the Al, Cr, and Ga analogues—while some analogues show little flexibility, such as the Fe and Sc analogues [15].

2.7 Mechanical Properties of Metal-Organic Frameworks

The mechanical properties of MOFs represent an area of great interest but relatively little research to date. The first reports on mechanical properties appeared only

about a decade ago [17]. A few known factors affect the mechanical properties of MOFs. Differences in bond strength within a single MOF, for example a combination of strong coordination bonds and weak hydrogen bonds, can produce flexibility in the structure. More connections between nodes within a MOF usually produces higher hardness and stiffness. Different connection geometries and topologies often result in different mechanical properties. Lastly, the presence of guest molecules affect mechanical properties greatly, especially in flexible MOFs [18].

Force can be applied to MOFs in a variety of modes—tension, compression, bending, torsion, shear, and combinations thereof. Different forces are applied to MOFs depending on their application. For example, gas sorption will involve hydrostatic compression where a MOF will require high bulk and shear moduli to resist deformation, collapse, and pressure-induced amorphization [17]. Figure 2.8 illustrates the different loading modes common to MOFs.

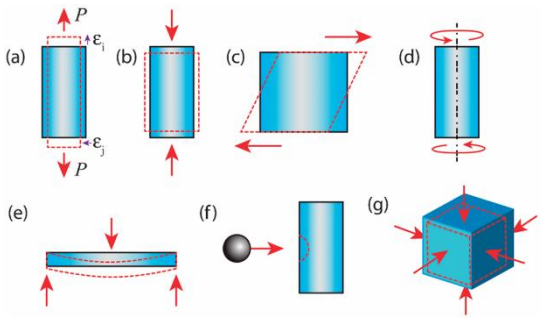

Figure 2.8: MOFs can be loaded in a) tension, b) compression, c) shear, d) torsion, e) bending, f) impact, and g) hydrostatic compression [17].

Two properties of particular interest in MOFs are the elastic modulus, which measures the ratio of applied stress to the resulting deformation in a material during uniaxial elastic deformation, and hardness, which measures a structure's resistance to plastic deformation. Elastic modulus is an intrinsic property, depending only on the material, whereas hardness is an extrinsic property, depending on both the microstructure

of the sample and material. However, since they both depend on the material, the two properties are not completely independent of one another. When plotting hardness and elastic modulus together, the properties of MOFs largely fall somewhere in the middle among metals, ceramics, and polymers, as seen in Figure 2.9.

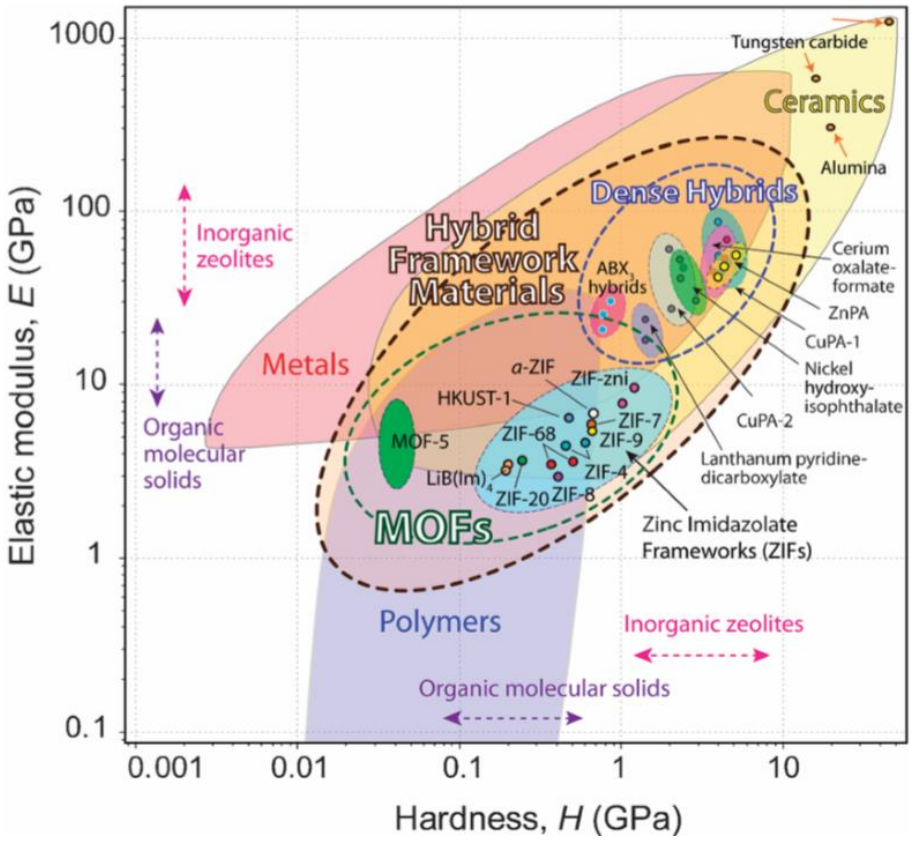

Figure 2.9: Plotting hardness versus elastic modulus, MOFs fall into the smaller dashed circle in the lower left, roughly centered among organic polymers, inorganic ceramics, and metals. MOFs here are shown in the greater context of hybrid framework materials, denoted by the larger dashed circle, which includes dense hybrids, denoted by the other smaller dashed circle [17].

The central location of MOF properties reinforces their organic-inorganic hybrid nature. The elastic modulus of MOF-5 highlights the anisotropy present even in some stiff MOFs. The ZIF series illustrates the wide range, larger than any series of dense hybrids, even a single series of MOFs can occupy with small changes to the organic linker and inorganic node.

2.8 Nanoindentation

Nanoindentation is a common method for measuring the elastic modulus of MOFs and possesses many advantages that make it ideal for MOFs. Sample preparation is minimal, multiple runs can be done on one sample, and operation of the nanoindenter itself is relatively simple. Nanoindentation systems can be extremely flexible with different possible tip geometries and a wide range of applied forces from kilo-newtons to pico-newtons [19]. The main challenges of nanoindentation are proper calibration and analysis of the data with an appropriate method.

The different tip geometries are appropriate for different material types and sizes. For example, spherical tips are generally better for brittle materials whereas sharp tips are better for ductile materials [19]. In the realm of sharp tips, the Berkovich tip is the most commonly used tip and is particularly good for indentation on a small scale [20]. Figure 2.10 shows a Berkovich tip.

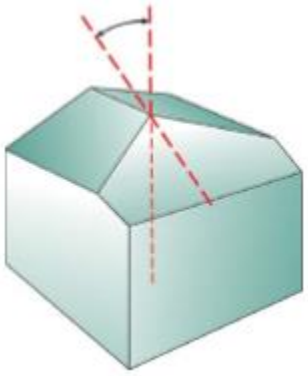

Figure 2.10: A Berkovich tip is a three-sided pyramid with a large tip angle to minimize friction during indentation. The tip maintains its geometry well even on very small scales [20].

The Oliver-Pharr method is commonly employed in nanoindentation of MOFs [21]. The method begins with the relation between load and displacement for punch geometries in Equation 2.1:

$$P = \propto h^m \tag{2.1}$$

where P is the indenter load, h is the elastic displacement of the indenter, and α and h are constants [21]. The constant m depends on the punch geometry. The elastic modulus is calculated through a value called the reduced modulus, E_r, as seen in Equation 2.2:

$$\frac{1}{E_r} = \frac{(1-v^2)}{E} + \frac{(1-v_i^2)}{E_i} \tag{2.2}$$

where E and v are the elastic modulus and Poisson's ratio of the sample and E_i and v_i are the elastic modulus and Poisson's ratio for the indenter [21]. The reduced modulus comes from analyzing a load-displacement curve like the one in Figure 2.11 based on an indent like the one illustrated in Figure 2.12.

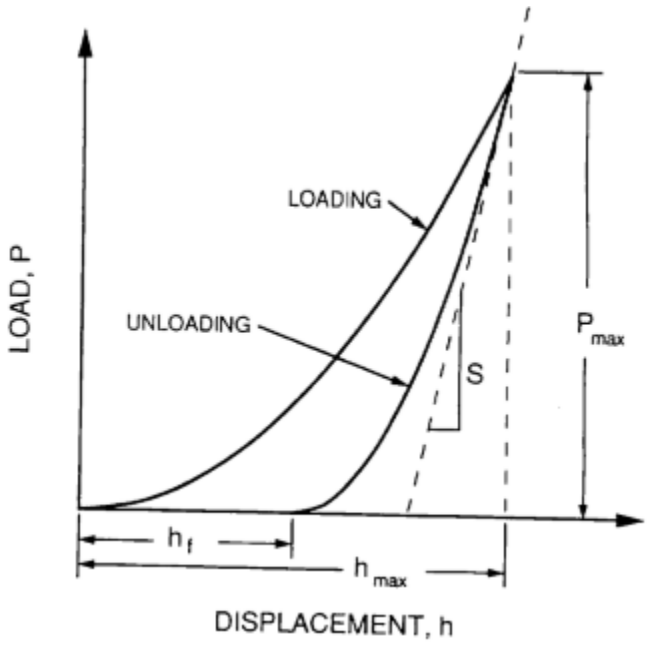

Figure 2.11: This plot exemplifies load-displacement curves. P_{max} is the peak indentation load, h_{max} is the indenter displacement at P_{max}, h_f is the depth of the indent after unloading, and S is the initial unloading stiffness [21].

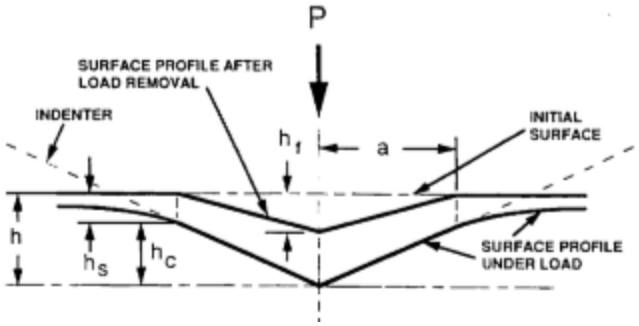

Figure 2.12: The surface profiles of interest are the initial surface profile, the profile under loading, and the profile after unloading. Values of interest include h_f, the depth of the indent after unloading, and h_c, the contact depth [21].

Information from the load-displacement curve is combined with the following equation to determine the reduced modulus:

$$S = \frac{dP}{dh} = \frac{2}{\sqrt{\pi}} E_r \sqrt{A} \tag{2.3}$$

where $S = \frac{dP}{dh}$ is the slope of the upper region of the unloading curve, representing the measured stiffness, and A is the area of elastic contact [21]. However, the area of elastic contact A is not ideal and often influenced by the contact depth h_c so that A is expressed a function of contact depth:

$$A = F(h_c) \tag{2.4}$$

$F(h_c)$, also known as the diamond area function (DAF), is obtained prior to experimentation by indentation of a sample with a known modulus, such as fused silica. The DAF maps the relation between the projected contact area and the contact depth at small magnitude, from about 10 nm to 1000 nm. During such small indentation depth, the blunt indenter tip can induce error when using the ideal indenter shape function to calculate the projected contact area.

The contact depth h_c itself is calculated from experimental data via a series of relations. First, the total displacement h during indentation is given by

$$h = h_c + h_s \tag{2.5}$$

where h_s is the displacement of the surface at the perimeter of contact with the sample. One value of h that can be experimentally determined is the total displacement at maximum load h_{max}. Rearranging for h_c:

$$h_c = h_{max} - h_s \tag{2.6}$$

The value of h_s depends on the indenter geometry. For a conical indenter:

$$h_s = \epsilon \frac{P_{max}}{S} \tag{2.7}$$

where P_{max} is the maximum load and ϵ has a value between 0 and 1 depending on the indenter geometry. The variable ϵ equals 0.75 for a Berkovich indenter. Putting everything together:

$$h_c = h_{max} - \epsilon \frac{P_{max}}{S} \tag{2.8}$$

Equation 2.3 can then be rearranged to solve for E_r with the data provided from indentation experiments and calculated values from previous equations.

$$E_r = \frac{\sqrt{\pi}}{2} \frac{S}{\sqrt{A}} \tag{2.9}$$

Including the DAF finally gives Equation 2.10.

$$E_r = \frac{S}{2\beta} \sqrt{\frac{\pi}{A}} \tag{2.10}$$

where β is introduced to correct the non-symmetrical indenter shape and equals 1.034 for a Berkovich indenter. Although the tip does not produce completely uniaxial stress, and the Oliver-Pharr method assumes an isotropic material, which many MOFs are not, the method still gives a good estimate of the properties [17]. However, the surface of the sample indented should ideally be as flat as possible so that the stress is largely produced in only one direction.

2.9 Mechanical Properties of MOF-5

Both empirical experimentation, mainly with nanoindentation, and theoretical calculations, such as with Density Functional Theory (DFT), are employed to obtain the mechanical properties of MOF-5. Nanoindentation by C.A. Bauer *et al.* gives an average elastic modulus of 2.7 ± 1.0 GPa. DFT calculations from the same group resulted in an average value of 21.6 GPa for the (100) and 7.5 GPa for the (111) [22]. They account for this discrepancy with the large anisotropic elastic response of MOF-5. The work of Vlassak *et al.* provides a correction factor to apply to the indentation modulus to account for elastic anisotropy [23]. Bauer *et al.* arrive at an elastic modulus of 7.9 GPa for the (100) of MOF-5 using this correction factor. This value is still significantly below the value calculated by DFT.

Bauer *et al.* provide three potential reasons for the discrepancy. First, the surface of MOF-5 as synthesized is rough. Surface roughness leads to underestimation of the elastic modulus when using area functions that assume a flat surface. Second, MOF-5 begins to break down very quickly in ambient conditions leading to a degradation of the mechanical properties. Third and most important, nanoindentation assumes the elastic properties of the sample do not change during loading and unloading. However, the open structure of MOF-5 deforms even under small loads in a manner analogous to buckling, creating a more compliant structure after nanoindentation [22].

Figure 2.13 overlays crystallographic directions with the structure of MOF-5 and shows the elastic modulus as a function of orientation. The <100> shows a much stiffer elastic response, as expected when compressing directly in line with the stiff BDC linkers [17].

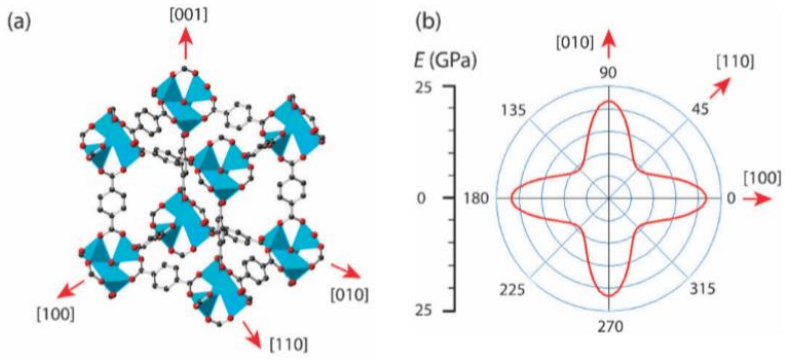

Figure 2.13: (a) The structure of MOF-5 is overlaid with directional axes. (b) Plotting elastic modulus as a function of orientation reveals that the response from the <100> is the stiffest, in line with expectation due to that direction being directly in line with the rigid BDC linkers [17].

2.10 Mechanical Properties of MIL-53

A.U. Ortiz *et al.* calculated the theoretical elastic modulus of MIL-53(Al) in its large pore form, denoted MIL-53(Al)-lp, using DFT [24]. Much like MOF-5, the elastic modulus of MIL-53 is strongly directional. However, the anisotropy of the flexible MIL-53 is even greater than that of the rigid MOF-5. Elastic moduli as low as 0.9 GPa and as high as 94.7 GPa are calculated for MIL-53(Al)-lp. Figure 2.14 depicts the calculated directional elastic modulus along with the elastic moduli when compressing in specific directions.

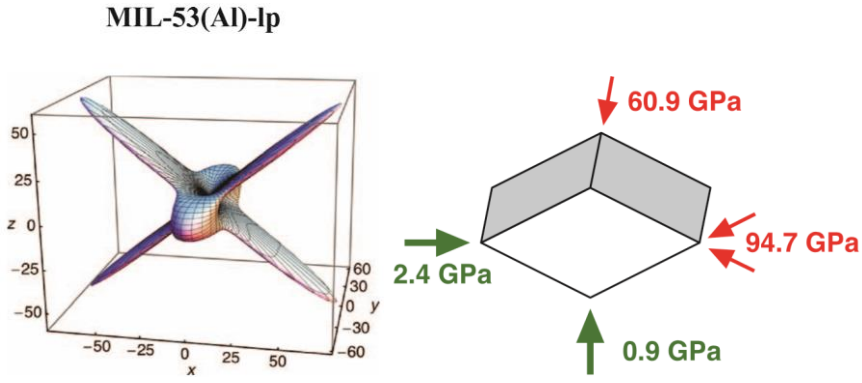

Figure 2.14: MIL-53(Al)-lp displays highly anisotropic elastic moduli. Values range from 0.9 GPa to 94.7 GPa. The figure on the right specifies the elastic modulus when compressing in specific directions [24].

2.11 Atomic Force Microscopy

Atomic Force Microscopy (AFM) is a scanning probe technique that provides topographical information about the surface of a sample. Images can range in size from 5 nm^2 to 100 μm^2 with high resolution [25]. Figure 2.15 compares the scale of AFM to other analytical techniques.

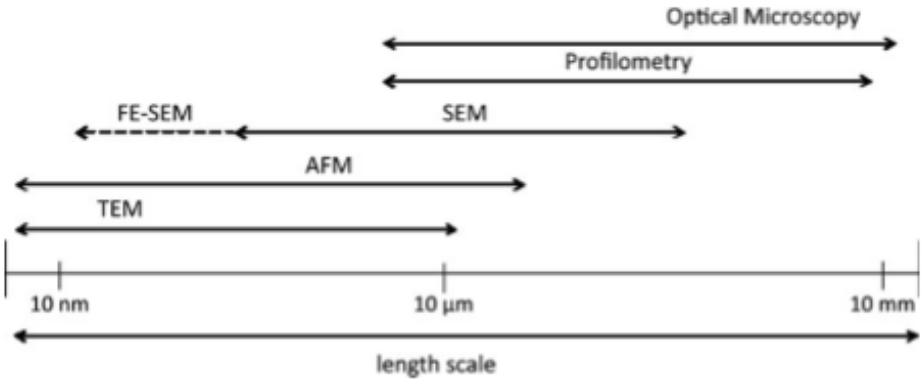

Figure 2.15: AFM provides a wide range of scanning capability from a hundred microns down to nanometers [25].

AFM employs a microfabricated cantilever that ends in a sharp tip used for scanning the sample surface. The cantilever, including the tip, usually consists of either silicon or silicon nitride. Figure 2.16 shows an SEM image of a typical AFM cantilever.

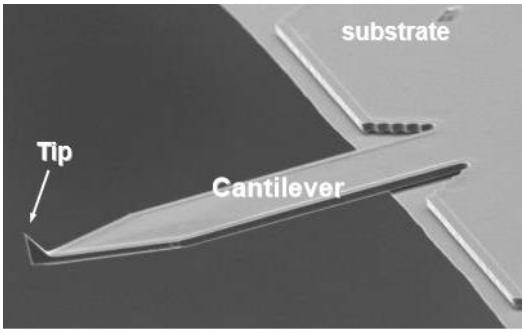

Figure 2.16: The AFM cantilever terminates in a sharp tip used for scanning the surface of a sample. The radius of the tips can be as small as 9 nm [26].

This tip scans across the surface of the sample, typically in a back-and-forth square raster pattern, acquiring height data. Changes in sample height cause changes in force between the tip and the sample surface and consequently deflection of the

cantilever. This deflection is measured via a laser that reflects off the back of the cantilever onto a four-quadrant photodiode. Figure 2.17 displays the deflection pattern of the laser off the cantilever while Figure 2.18 illustrates how the photodiode detects cantilever deflection.

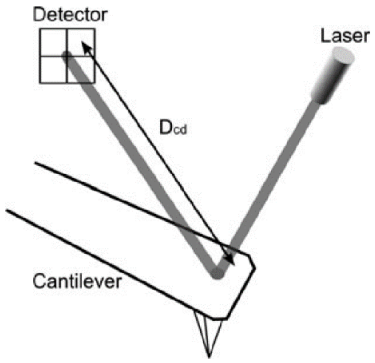

Figure 2.17: The laser reflects off of the cantilever into the detector in order to allow tracking of cantilever deflection [25].

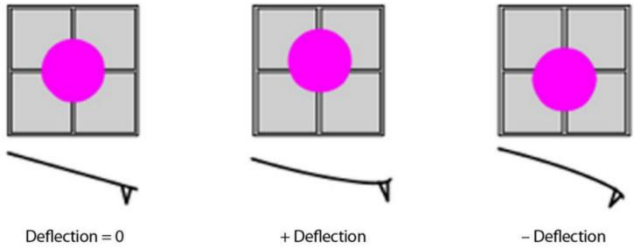

Figure 2.18: The laser is generally centered so that all four quadrants receive equal light at zero cantilever deflection**.** Changes in light received, and thus voltage generated, by the upper or lower half of the four-quadrant photodiode allow for detection of cantilever deflection [27].

The AFM uses this detection scheme in order to adjust the height of the tip appropriately to maintain constant force between the tip and the sample surface. Constant force also means that the tip-sample distance remains constant [25]. Piezoelectric elements control the scan across the surface and the height adjustment as well as measuring the force between the tip and sample, as seen in Figure 2.19.

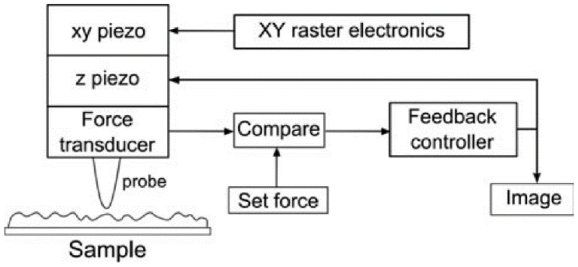

Figure 2.19: An AFM employs piezoelectric elements to move the tip across the sample surface, to adjust the tip height in response to sample height changes, and to measure the tip-sample force. These measurements and adjustments allow the AFM to maintain constant force between the tip and sample and consequently constant tip-sample distance [25].

The AFM then produces height data by tracking the voltage applied to the z-piezo, producing an image of the sample surface [25]. This method produces genuine three-dimensional data, which is not usually available from optical microscopy techniques.

AFM has several different modes of imaging depending on how the tip interacts with the surface. Contact mode, very naturally, involves continuous contact with the surface. The AFM can also image in "tapping mode" using intermittent contact with the surface. This intermittent contact reduces damage to soft samples and better maintains the tip apex from dulling or picking up particles [27]. Tapping mode is established by exciting the cantilever actuator with a voltage that the piezoelectric actuator turns into an oscillatory motion. The actuator is excited in such a way as to cause the cantilever to oscillate at or near its fundamental frequency in a manner approximated by a simple harmonic oscillator. Figure 2.20 shows the first four vibrational modes of a typical cantilever.

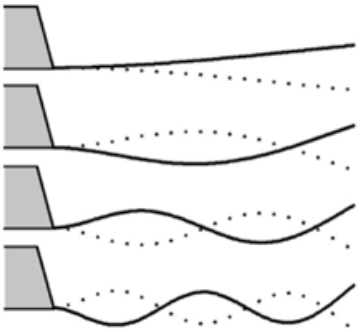

Figure 2.20: The first four vibrational modes of a typical cantilever are shown in order here. AFM uses the fundamental mode for regular tapping mode topography imaging [28].

In contrast to contact mode, the value held constant in tapping mode is the vibration amplitude, not the tip-sample height [27]. Tapping mode is also known as AC mode for this reason [29].

2.12 Amplitude Modulation – Frequency Modulation (AMFM)

AFM has many different modes that provide information in addition to simple topography. One of these, called AMFM, measures mechanical information about the sample. AMFM gets its name from its manner of operation. AMFM operates by exciting the cantilever at two resonances simultaneously—the fundamental frequency and usually the second but also possibly the third or fourth resonance. AM stands for amplitude modulation, referring to the first resonance employed for regular tapping mode imaging. FM stands for frequency modulation, referring to the higher mode resonance that provides information on tip-sample interaction used to determine mechanical properties [30].

Analysis of the tip-sample interaction begins with Equation 2.11 matching the excitation frequencies of the forces driving the cantilever and the first two resonances of the cantilever.

$$F_{exc} = F_1 \cos \omega_1 t + F_2 \cos \omega_2 t \tag{2.11}$$

where F_i and ω_i are the excitation force and angular frequency of a particular resonance i, respectively, and t is time [31]. The angular frequency ω is related to ordinary frequency f by $\omega = 2\pi f$. The relation of the input driving forces leads to Equation 2.12 describing the cantilever response to the excitation forces.

$$z = z_0 + A_1 \cos(\omega_1 t - \phi_1) + A_2 \cos(\omega_2 t - \phi_2) \tag{2.12}$$

where ϕ_i and A_i are the phase shift and amplitude of a particular resonance i, respectively [31]. Figure 2.21 illustrates the inputs and outputs when exciting a cantilever at two resonances.

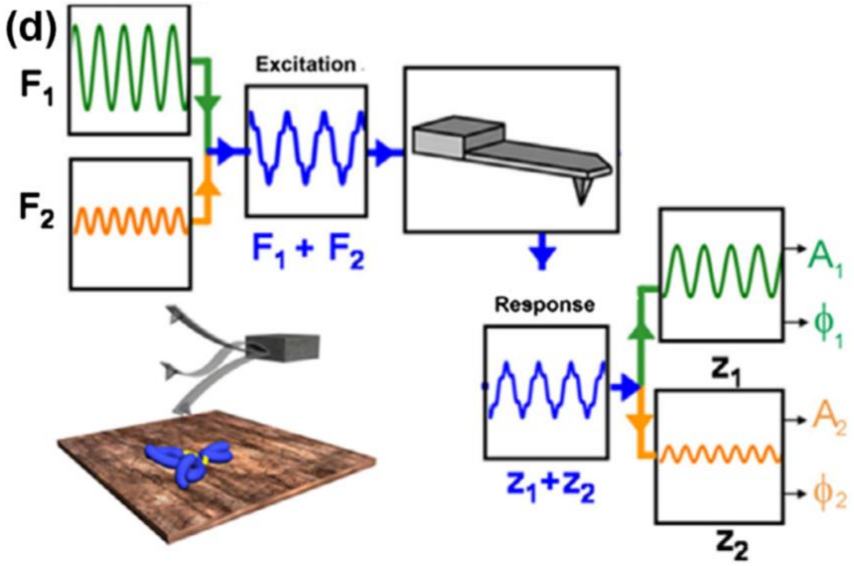

Figure 2.21: Excitation forces excite the cantilever at its two resonances. The AFM detects the resulting amplitudes A_i and phase shifts ϕ_i [31].

The phase shift in the second resonance is used to measure the elastic modulus through a series of mathematical relations. First, Equation 2.13 employs an analytic relationship to obtain the gradient of the force between the tip and sample from the phase shift of the second mode.

$$F'_{ts,peak}(z_c) \approx C \frac{k_2 A_{0,2}}{Q_2 A_2(z_c)} \cos \phi_2(z_c) \tag{2.13}$$

where C is the cantilever response in contact with a surface, $A_{0,2}$ is the amplitude of the second resonance at a reference position, Q_2 is the quality factor of the second resonance, and k_2 is the force constant of the second resonance [31]. Next, the frequency shift is calculated from Equation 2.14.

$$\Delta f_2 = -f_{0,2}\frac{\langle F_{ts} z \rangle}{k_2 A_2^2} \tag{2.14}$$

where F_{ts} is the integral of F'_{ts}, $f_{0,2}$ is second resonant frequency at a reference position, and Δf_2 is the frequency shift of the second resonance while the tip interacts with the surface [31]. The frequency shift is then used to approximate a tip-sample stiffness in Equation 2.15.

$$k_{ts} \approx \frac{2k_2 \Delta f_2}{f_{0,2}} \tag{2.15}$$

The tip-sample stiffness can also be calculated using a mechanical model such as a Hertz punch indenter, which approximates the shape of an AFM tip, shown in Equation 2.16 [31].

$$k_{ts} = 2E_{eff} r_c \tag{2.16}$$

where r_c is the contact radius of the tip. Putting together Equations 2.15 and 2.16 and rearranging allows for calculation of the effective elastic modulus in Equation 2.17.

$$E_{eff} = \frac{k_2 \Delta f_2}{f_{0,2} r_c} \tag{2.17}$$

where r_c is the contact radius of the punch. Finally, the effective elastic modulus is used to calculate the sample elastic modulus through Equation 2.18.

$$\frac{1}{E_{eff}} = \frac{1 - v_t^2}{E_t} + \frac{1 - v_s^2}{E_s} \tag{2.18}$$

where E_t is the elastic modulus of the tip, ν_t is the Poisson's ratio of the tip, and ν_s is the Poisson's ratio of the sample. Poisson's ratio is generally estimated to be 0.3 for hard materials and 0.4 for soft materials.

During AMFM, a lock-in amplifier measures the phase and amplitude of the second resonance from the photodiode signal [30]. In response to any changes in phase or amplitude, an automatic gain control circuit modulates the drive voltage in order to keep the amplitude constant while a phase-locked loop adjusts the drive frequency to keep the phase at 90° [32]. The resulting changes in drive frequency and drive voltage provide information on the elastic tip-sample interaction and loss, respectively. Following Equations 2.17 and 2.18, a higher drive frequency shift will equate to a larger elastic modulus. Figure 2.22 builds on Figure 2.21 by highlighting the information provided by the different values measured during AMFM.

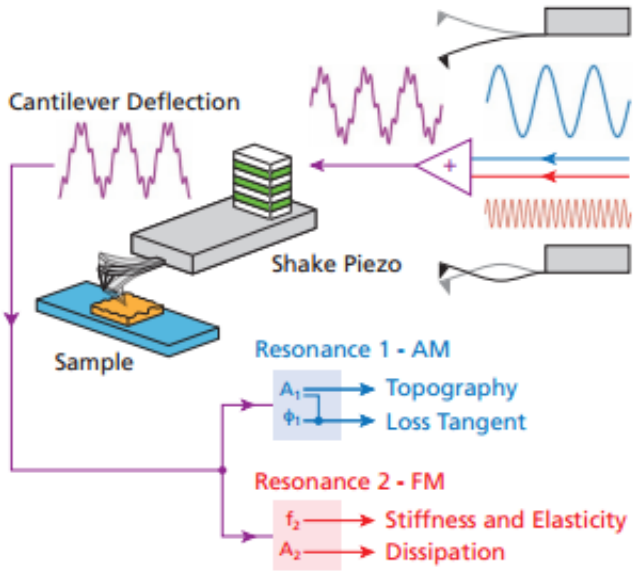

Figure 2.22:.The first resonance, shown in blue, provides topographical information available with normal AFM. The second resonance, shown in red, provides mechanical information such as elastic modulus, stiffness, and dissipation [32].

The contact radius of the tip can be determined either directly by measuring the radius of the tip or by measuring a sample of known modulus and adjusting the contact

radius in the AFM software until the expected modulus is measured [32]. If the latter option is employed, the reference sample should have a similar modulus to the test sample for the most accurate results.

AMFM maps an image of the mechanical properties in a non-destructive manner like AFM does with topography. Figure 2.22 provides two examples of topography and elastic modulus maps provided by AMFM.

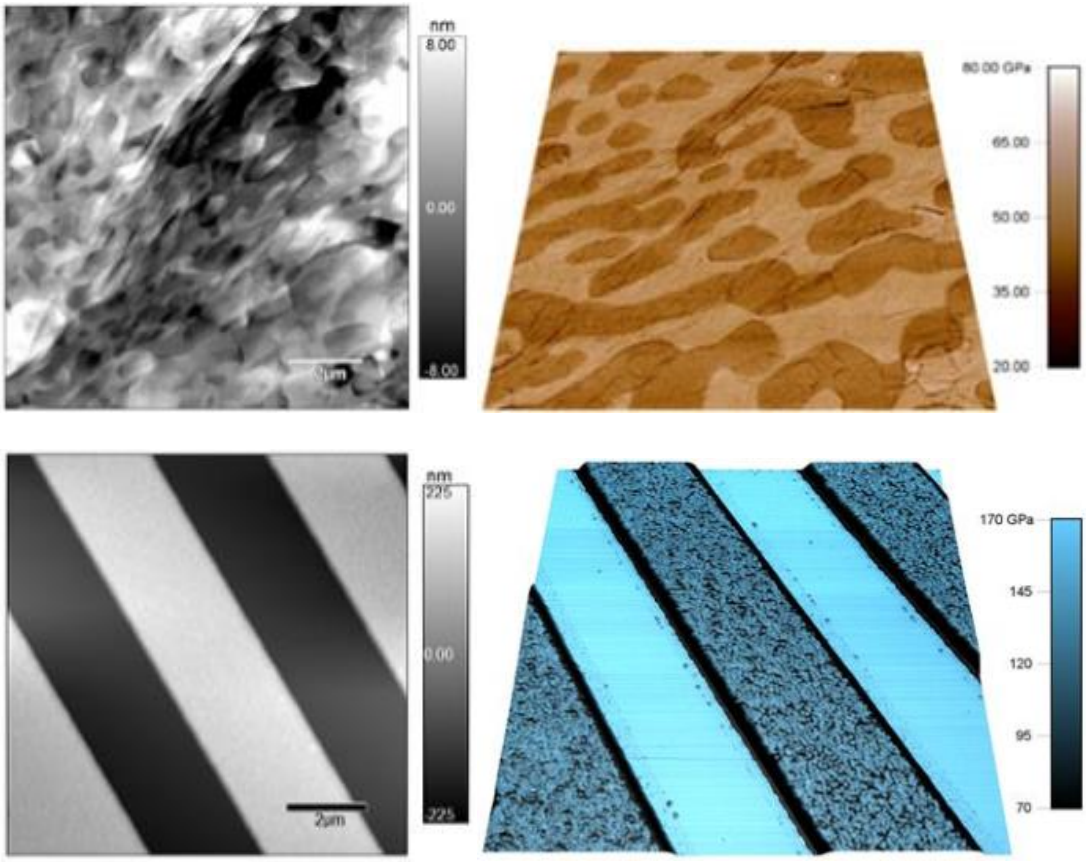

Figure 2.22: The top AMFM images are the topography map (right) and elastic modulus map (left) of a 50/50 lead-tin solder. The bottom images belong to a 200 nm patterned titanium film on silicon [33].

AMFM provides more reliable measurements on samples with surface roughness not exceeding a micrometer. The photodiode has difficulty accurately tracking rapid, large changes in deflection, and the z-piezo cannot always adjust quickly enough for these rapid and large changes in height.

Chapter 3: Experimental

3.1 Synthesis of MOF-5

Synthesis of MOF-5 was based on the work of B. Panella and M. Hirscher [12]. 0.15 g of zinc nitrate hexahydrate was weighed out and added to 5 mL of N,N-dimethylformamide (DMF). 0.04175 g of terephthalic acid was weighed out and added to the solution. The solution was stirred for 10 minutes in order to dissolve the solid. 0.275 mL of trimethylamine (TEA) was then added drop by drop to the solution, and the solution was stirred for 45 minutes. The solution was filtered using filter paper, a funnel, and a beaker. A wet, white slurry was left on the filter paper. The white slurry was thoroughly rinsed while still wet with three rinsings of 10 mL DMF for a total of 30 mL of DMF. The wet solid was dried in an oven at 100 °C for 3 hours, resulting in brittle, white product.

3.2 Synthesis of MIL-53(Al)

The synthesis of MIL-53(Al) was based on Loiseau *et al.* [16]. MIL-53(Al) was prepared by mixing 0.576 g of terephthalic acid, 2.60 g of aluminum nitrate nonahydrate, and 10.0 mL of deionized water in a 45 mL Parr acid digestion vessel, model 4744. The acid digestion vessel was heated at 220 °C for 3 days. The pressure vessel was cooled to room temperature in one hour using a small fan. The white product was filtered using filter paper and washed repeatedly with deionized water. The product was then purified by heating at 330 °C for 3 days.

3.3 Immobilizing MIL-53(Al)

Both photoresist and epoxy were separately used to immobilize MIL-53(Al) particles. For photoresist, MIL-53(Al) particles were immobilized in MicroPosit® S1813®

photoresist. The MIL-53(Al) particles were placed in S1813 photoresist on glass slides and then spread until the photoresist forms a thin layer with MIL-53(Al) particles trapped throughout the photoresist. The composites were then heated to 115 °C for 10 minutes on a hotplate to hard bake the samples.

The S1813 samples were polished using a two-step polishing process. The samples were first polished on a 5 μm α-alumina slurry polishing wheel. Then the samples were polished on a 0.3 μm α-alumina slurry polishing wheel. The samples were rinsed with deionized water after each polishing step to avoid contamination. After polishing, the samples were dried at 115 °C for 10 minutes to dehydrate the samples again.

To immobilize the MOFs in epoxy, Buehler EpoThin® epoxy resin and Buehler EpoThin® epoxy hardener were used. First, a Buehler epoxy mold was filled with resin and hardener in a ratio of 100 parts resin to 39 parts hardener. MIL-53(Al) particles were then added on top of the epoxy. The epoxy was allowed to cure for at least 9 hours.

The epoxy samples were polished in two steps. First, 600 grit sandpaper was used to polish down the rough surface of the epoxy. Then, a 0.3 μm α-alumina slurry polishing wheel was used to polish the surface to a mirror-like finish.

The polished epoxy puck containing MIL-53(Al) was diced in half from top to bottom with a Buehler IsoMet® low speed wafering saw, resulting in two half-moon shapes. Excess epoxy was diced off the back of the two samples using the same Buehler saw, and the samples were cleaned by sonicating with IPA for 1 minute and then DI water for 1 minute. Finally, the samples were attached to a glass slide using two-sided tape in preparation for AMFM and nanoindentation.

3.4 Optical Microscopy

Optical microscope pictures were taken using a Leica DMRB microscope. Magnification ranged from 5x to 50x.

3.5 X-ray diffraction

θ-2θ scans were carried out with a Bruker D8 Discover x-ray diffractometer using Cu Kα radiation. MOF-5 samples was scanned from 5° to 55° at 2°/min with a 0.03° increment. MIL-53(Al) samples were scanned from 5° to 50° at 2°/min with a 0.03° increment. The voltage and current on the tube were 40 kV and 40 mA, respectively.

3.6 AFM and AMFM

AFM and AMFM images were taken with an Asylum Research MFP-3D atomic force microscope. AC-160TS-R3 cantilevers were placed in a 3D standard cantilever holder for AFM and a 3D AMFM cantilever holder for AMFM. Scan sizes ranged from 1 micron to 20 μm. Scan rates ranged from 0.5 Hz to 1.0 Hz.

3.7 Nanoindentation

A MicroMaterials NanoTest Vantage was utilized to carry out the nanoindentation experiments using a diamond Berkovich indenter at 26 °C. For each indentation, the material was first indented to a maximum load of either 2 mN, 1 mN, or or 0.5 mN with a loading rate of 0.1 mN/s. The maximum load was held constant for a 20-second dwell period before it was unloaded. The unloading rate was 0.1 mN/s. The elastic modulus and Poisson's ratio of the diamond indenter were 1141 GPa and 0.07, respectively. The Poisson's ratio for the samples was assumed to be 0.3.

3.8 SEM

SEM images were taken with a Helios NanoLab 650 high resolution SEM at the Oregon State University Electron Microscopy Facility. Images were taken at 5 kV.

3.9 Thermogravimetric Analysis

Thermogravimetric Analysis (TGA) runs were carried out with a Q500 TGA from 40 °C to 595 °C at a heating rate of 5 °C/min, showing the percent weight loss from MOFs at different temperatures over this temperature range.

3.10 PowderCell 2.4

Diffraction patterns were indexed using diffraction simulations in PowderCell 2.4 based on Bragg-Brentano geometry and Cu Kα radiation.

Chapter 4: Results and Discussion

4.1 Synthesis of MOF-5

Synthesis of MOF-5 required optimizing the amount of washing with DMF to yield phase pure material in order to completely remove unreacted precursor. Insufficient washing resulted in phase impure MOF-5. Figure 4.1 plots the diffraction patterns of both the phase impure and phase pure MOF-5.

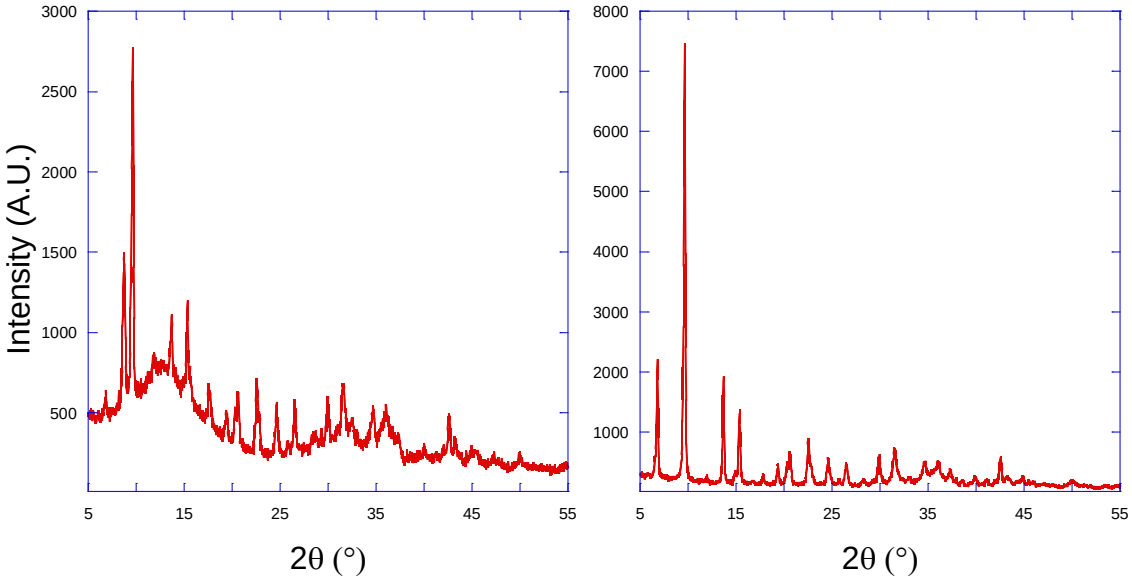

Figure 4.1: Insufficient washing of MOF-5 with DMF results in phase impure MOF-5 as seen in the diffraction pattern on the left. The broad peaks from 10 to 20 degrees and 30 to 40 degrees as well as the presence of extraneous peaks indicate phase impurity. The diffraction pattern of phase pure MOF-5 appears on the right.

MOF-5 came out of drying for 3 hours as a white, brittle material. The diffraction pattern of phase pure MOF-5 from the work of Panella *et al.* confirmed the successful synthesis of MOF-5 as seen in Figure 4.2.

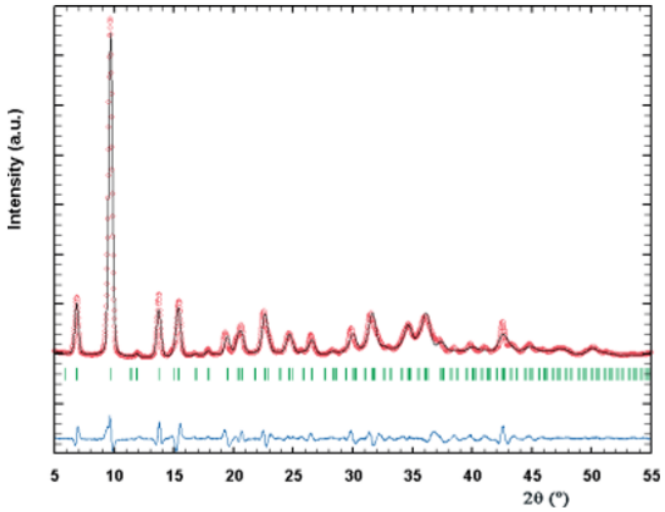

Figure 4.2: The diffraction pattern of phase-pure MOF-5 from Panella *et al.* is shown in red [12].

MOF-5 deteriorated within hours in ambient conditions due to the presence of water vapor. Bauer *et al.* noted that the mechanical properties of MOF-5 measured in as few as 4 hours after exposure to ambient conditions differed greatly from properties measured within 1 hour [22]. XRD of the MOF-5 samples synthesized for this project, seen in Figure 4.3, revealed a corresponding deterioration of the structure of MOF-5 within 6 hours of exposure to ambient conditions after the drying step.

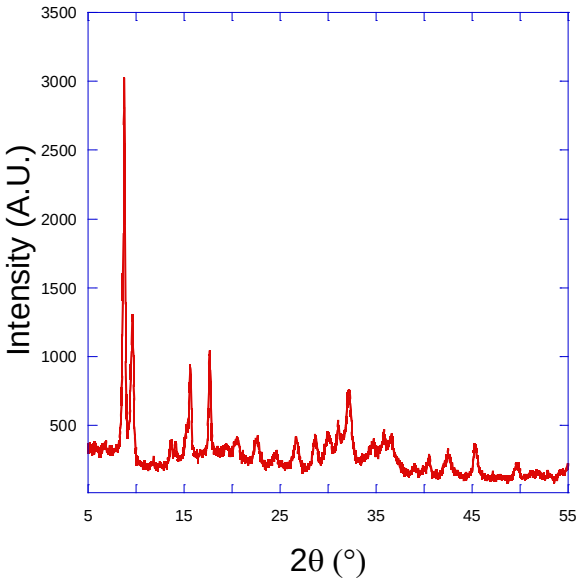

Figure 4.3: This diffraction pattern of MOF-5 was taken 6 hours after synthesis and drying.

MOF-5 breaks down within hours of exposure to ambient conditions due to the presence of water vapor. For this reason, measurements of the properties of MOF-5 have to be carried out very quickly after exposure to ambient conditions.

4.2 Synthesis of MIL-53(Al)

Synthesis of MIL-53(Al)-lt was successful. XRD was used to confirm the structure of MIL-53(Al) at two points. First, XRD was performed on MIL-53(Al)-as shown in Figure 4.4.

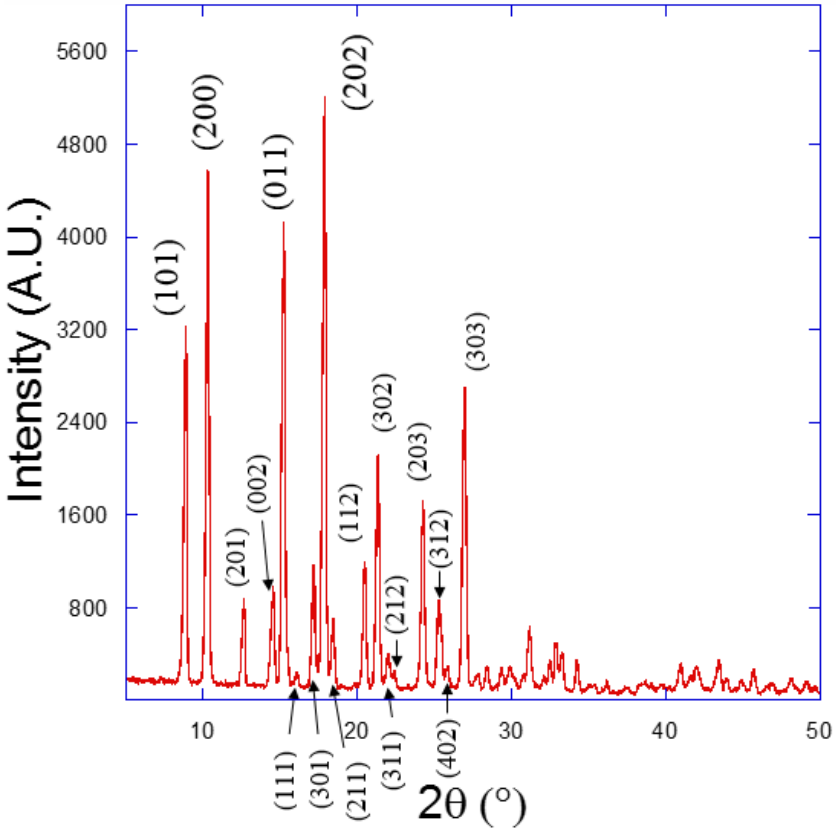

Figure 4.4: MIL-53(Al)-as still has BDC trapped in its pores. The above diffraction pattern corresponds to the state of MIL-53(Al) before the drying step drives the BDC out of the pores.

The diffraction pattern of MIL-53(Al)-as from the work of Loiseau *et al.* in Figure 4.5 matches the diffraction pattern of the MIL-53(Al)-as from this project.

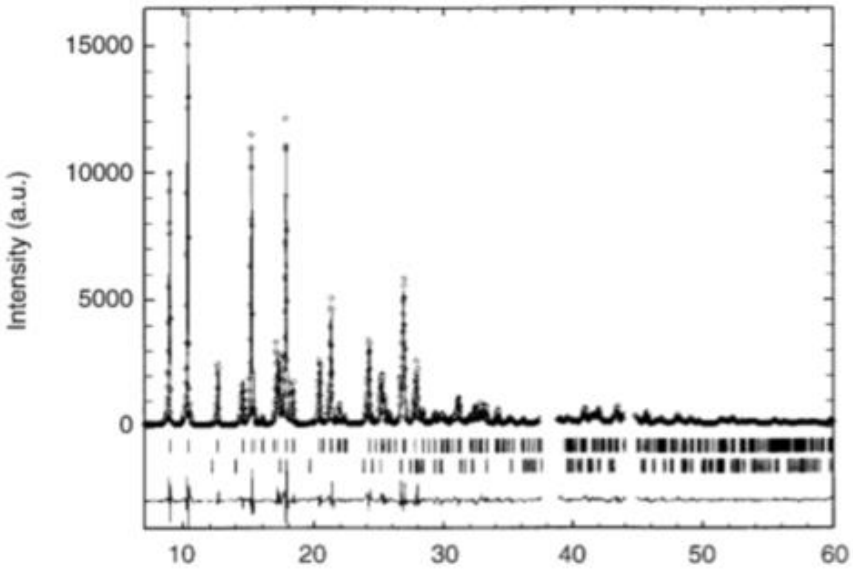

Figure 4.5: The diffraction pattern of MIL-53(Al)-as from the work of Loiseau *et al*. matches the diffraction pattern of MIL-53(Al)-as from this project [16].

XRD was carried out a second time after drying at 330°C for 3 days and cooling down to room temperature, which produces MIL-53(Al)-lt as seen in Figure 4.6.

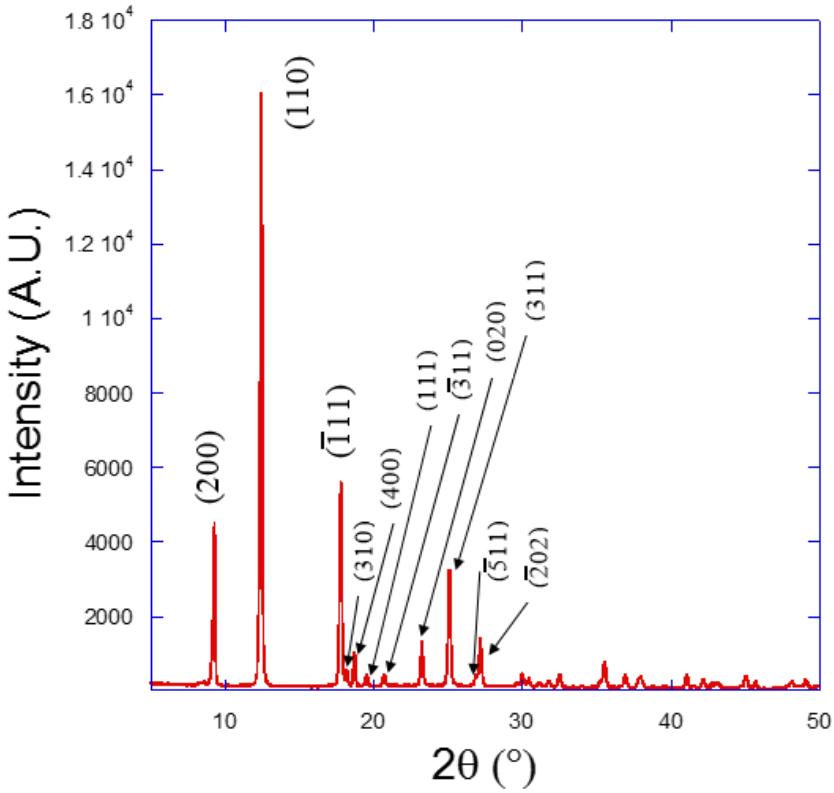

Figure 4.6: Drying MIL-53(Al)-as at 330°C for 3 days and cooling to room temperature results in MIL-53(Al)-lt. MIL-53(Al)-lt has water trapped in its pores.

The diffraction pattern of MIL-53(Al)-lt was compared to the diffraction pattern from the work of Loiseau *et al*. shown in Figure 4.7.

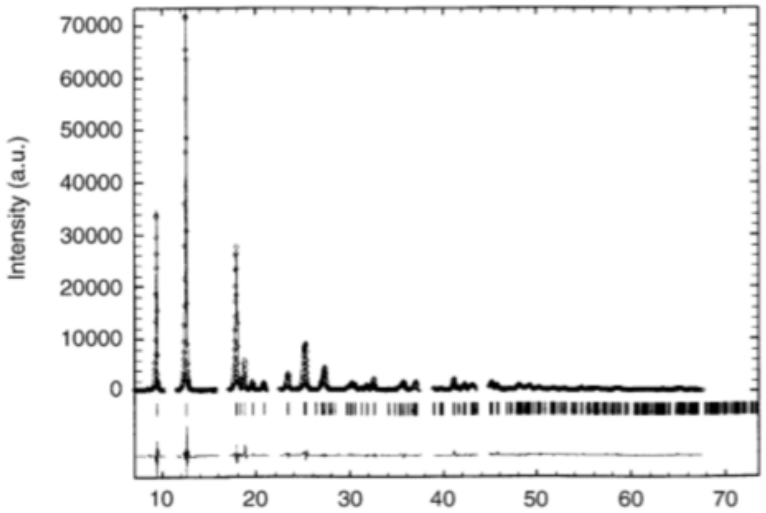

Figure 4.7: The diffraction pattern of MIL-53(Al)-lt from the work of Loiseau *et al.* was used to confirm successful synthesis and drying to obtain MIL-53(Al)-lt [16].

The diffraction pattern from the MIL-53(Al)-lt synthesized for this project matched the pattern in Loiseau *et al.* The procedure for synthesizing MIL-53(Al) had been altered from the work of Loiseau *et al.* for a 45 mL pressure vessel rather than the 23 mL pressure vessel used in the original work [16]. Attempting to synthesize MIL-53(Al) in a 45 mL pressure vessel using the mass of reagent in the original work of Loiseau *et al.* resulted in failure to synthesize MIL-53(Al) as seen in Figure 4.8.

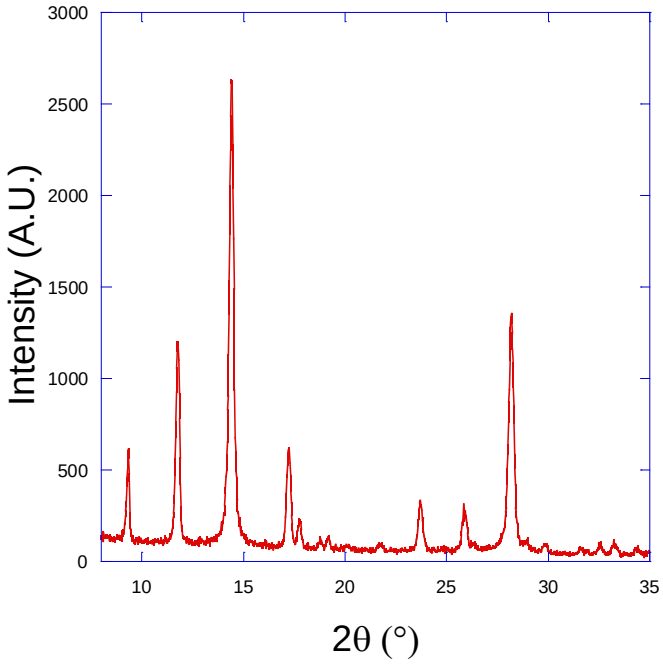

Figure 4.8: Attempting to synthesize MIL-53(Al) in a 45 mL pressure vessel with the amounts described by Loiseau *et al.* did not result in the MIL-53(Al) structure.

The difference in pressure vessel size changes the amount of reagents required to achieve the desired pressure inside the vessel. To account for the pressure vessel size difference, the mass of the reagents was doubled as well as the volume of deionized water. This change resulted in successful synthesis of MIL-53(Al).

The patterns of MIL-53(Al)-as and MIL-53(Al)-lt from this work were indexed out to 30 degrees using PowderCell 2.4, a diffraction simulation program. The work of Loiseau *et al.* provided atomic coordinates, crystal system, space group, and unit cell dimensions [16]. With this information, PowderCell calculated the expected diffraction pattern for the material and indexed that pattern in accordance with the d-spacing equation appropriate to the crystal system—orthorhombic for MIL-53(Al)-as and monoclinic for MIL-53(Al)-lt. These generated patterns were then matched to peaks from the experimental data in Figures 4.4 and 4.6. Figures 4.9 and 4.10 give the generated diffraction patterns for MIL-53(Al)-as and MIL-53(Al)-lt, respectively.

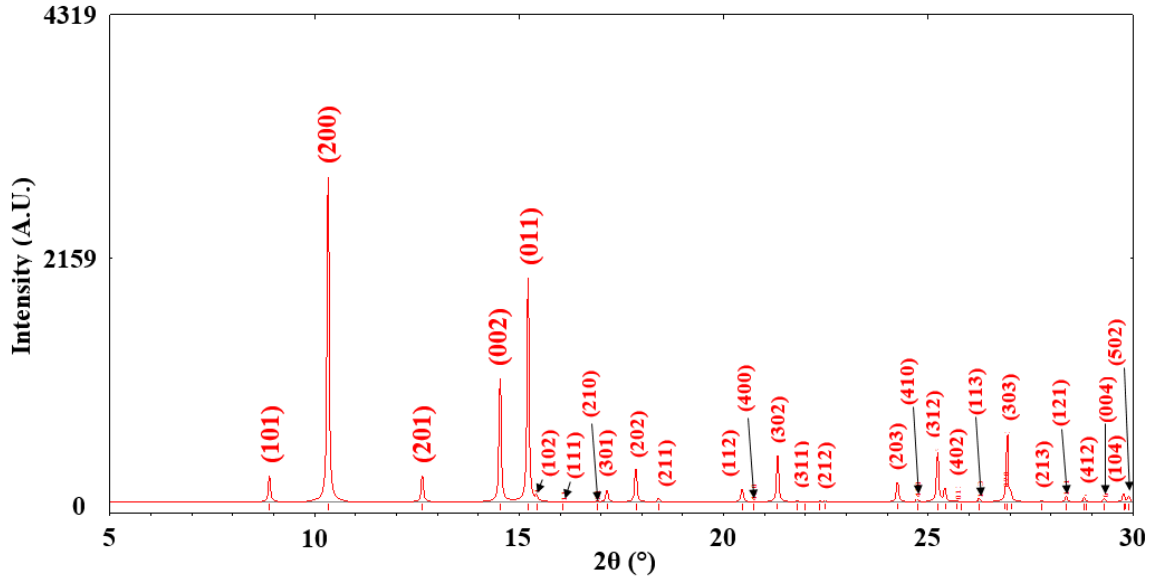

Figure 4.9: PowderCell generated and indexed a pattern for MIL-53(Al)-as.

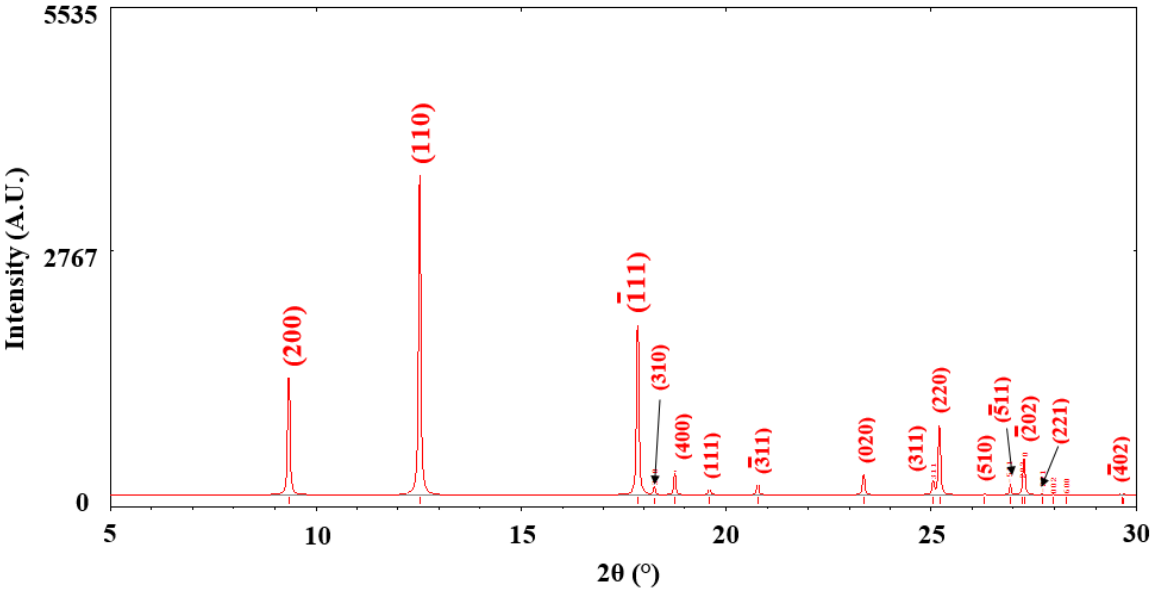

Figure 4.10: PowderCell generated and indexed a pattern for MIL-53(Al)-lt.

PowderCell generated extraneous peaks, so the 2θ positions of the peaks from the experimental data were compared to the 2θ positions calculated by PowderCell in order to index the experimental data. Tables 4.1 and 4.2 record the 2θ positions calculated by PowderCell compared to the experimental data for MIL-53(Al)-as and MIL-53(Al)-lt, respectively.

MIL-53(Al)-as		
Experimental 2θ (°)	Calculated 2θ (°)	hkl (PowderCell)
8.8939	8.901	(101)
10.305	10.32	(200)
12.617	12.624	(201)
14.538	14.531	(002)
15.229	15.205	(011)
16.07	16.065	(111)
17.15	17.137	(301)
17.871	17.855	(202)
18.441	18.42	(211)
20.483	20.453	(112)
21.354	21.313	(302)
21.984	21.8	(311)
22.405	22.38	(212)
24.266	24.238	(203)
25.287	25.23	(312)
25.887	25.405	(402)
26.938	26.922	(303)

Table 4.1: The experimental 2θ and 2θ calculated by PowderCell were compared for peaks in order to rule out extraneous peaks. This table compares 2θ for MIL-53(Al)-as.

MIL-53(Al)-lt		
Experimental 2θ (°)	Calculated 2θ (°)	hkl (PowderCell)
9.2634	9.344	(200)
12.416	12.525	(110)
17.76	17.855	(-111)
18.181	18.257	(310)
18.691	18.752	(400)
19.501	19.584	(111)
20.702	20.775	(-311)
23.225	23.353	(020)
25.086	25.052	(311)
26.857	26.926	(-511)
27.158	27.219	(-202)

Table 4.2: This table compares 2θ from experimental data and PowderCell for MIL-53(Al)-lt.

Not all batches of MIL-53(Al)-lt displayed complete phase purity. Figure 4.11 provides the pattern of one such batch.

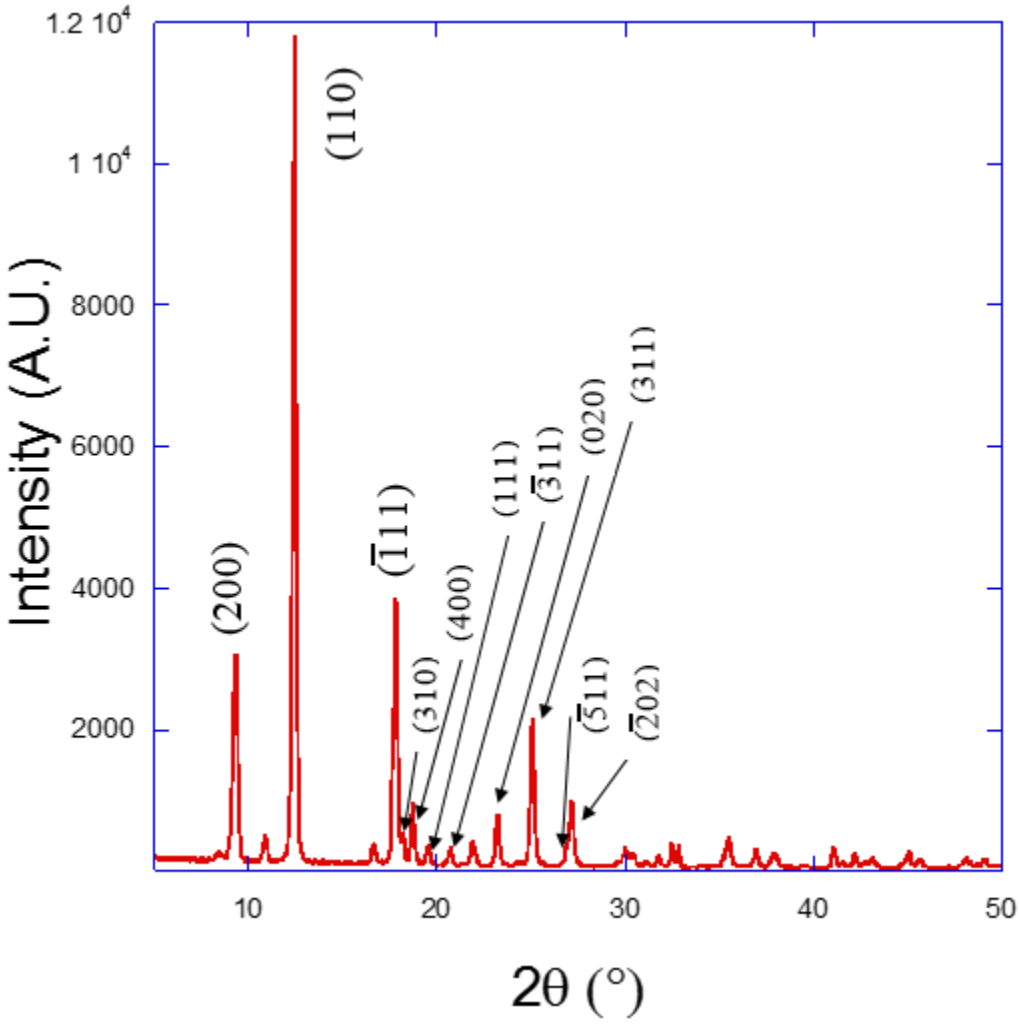

Figure 4.11: Extraneous peaks appeared at 10.9, 16.8, and 21.9 degrees in some batches of MIL-53(Al)-lt.

In order to understand why these extraneous peaks appeared, TGA was carried out on a sample of MIL-53(Al)-lt from these batches. The result is shown in Figure 4.12.

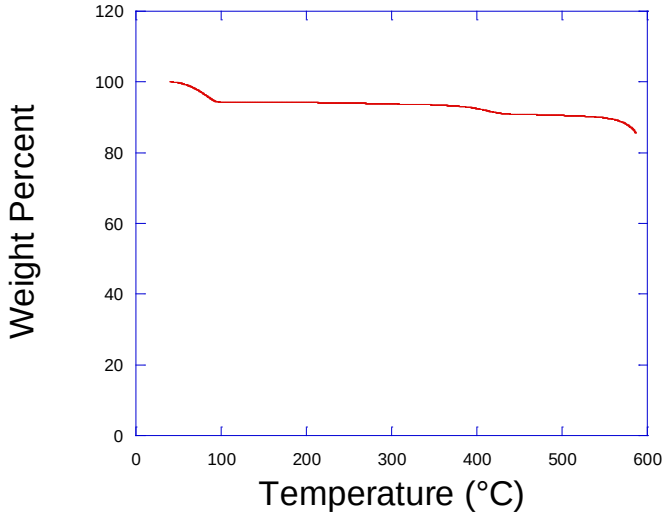

Figure 4.12: TGA was carried out on MIL-53(Al)-lt in order to discern why extraneous peaks sometimes appeared in the diffraction pattern of MIL-53(Al)-lt.

The results of the TGA run were compared to TGA runs of MIL-53(Al)-as and MIL-53(Al)-lt from Loiseau *et al*. shown in Figure 4.13.

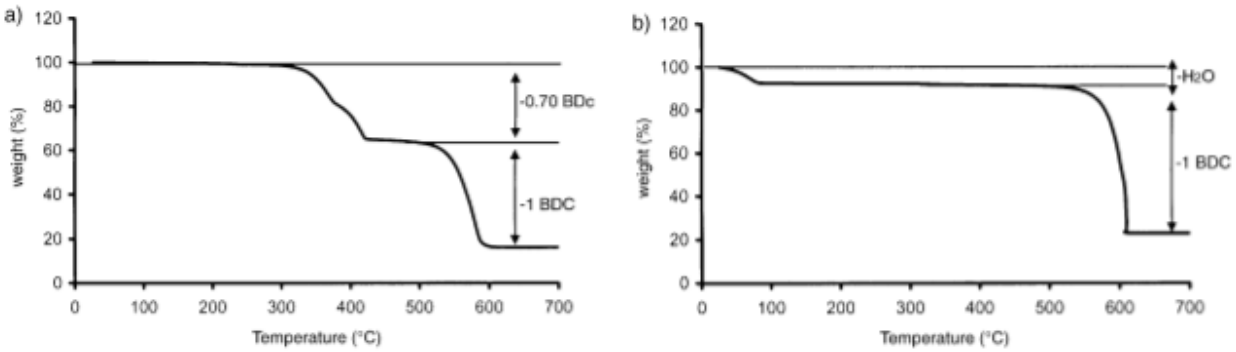

Figure 4.13: (a) TGA on MIL-53(Al)-as shows two distinct weight losses. First, the BDC molecules trapped in the pores of MIL-53(Al)-as, amounting to 0.70 equivalents of BDC, are expelled. Second, the BDC molecules making up the linkers of MIL-53(Al) break down, leaving Al_2O_3. (b) TGA on MIL-53(Al)-lt shows two weight losses. First, water trapped in the pores of MIL-53(Al)-lt is expelled. Second, the BDC molecules making up the linkers of MIL-53(Al) break down [16].

TGA of MIL-53(Al)-lt for the phase impure batches appeared to be a combination of the TGA for MIL-53(Al)-as and MIL-53(Al)-lt. Specifically, the TGA of MIL-53(Al)-lt from Figure 4.10 showed the weight loss associated with water loss from the pores of MIL-53(Al)-lt but also a small weight loss over the temperature range associated with the removal of BDC from the pores of MIL-53(Al)-as. This observation is corroborated by

the fact that the small peaks in phase impure MIL-53(Al)-lt diffraction pattern at 10.9 and 21.9 degrees correspond to the large (200) and (311) peaks from the diffraction pattern of MIL-53(Al)-as. Therefore, the activation of MIL-53(Al)-as was incomplete with some MIL-53(Al)-as failing to have the BDC trapped in its pore expelled during drying.

SEM was carried out on the MIL-53(Al)-lt particles. SEM revealed particles ranging in size from 1 to 5 microns as seen in Figures 4.14 and 4.15.

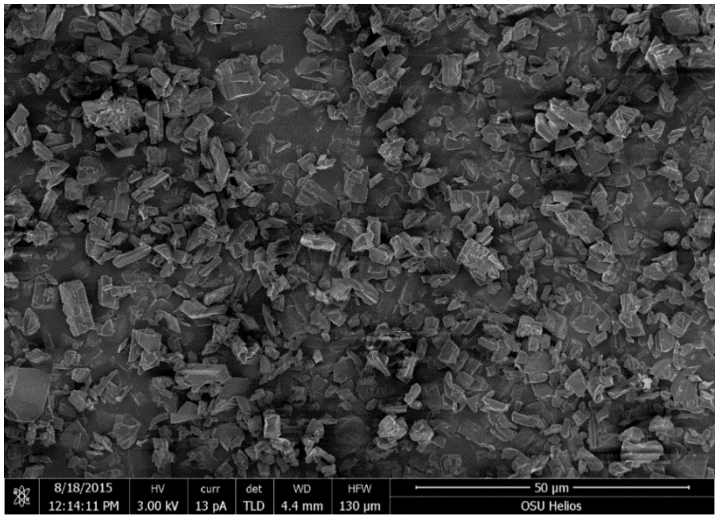

Figure 4.14: A large area SEM scan revealed a diverse array of particle sizes and shapes.

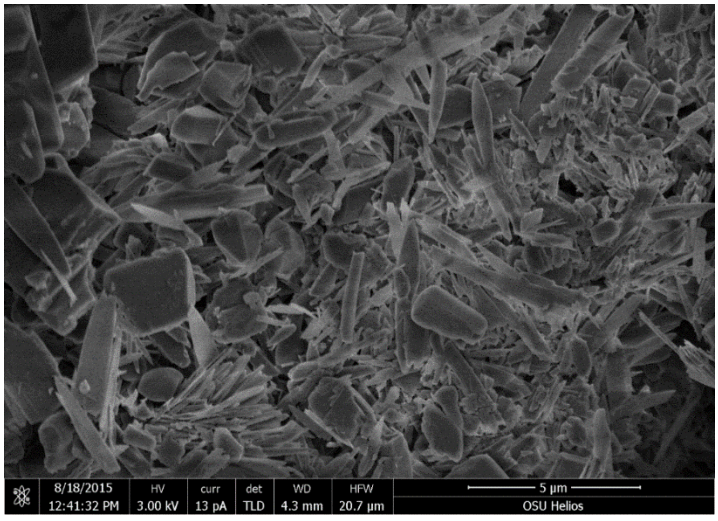

Figure 4.15: Scanning a smaller area showed that the MIL-53(Al)-lt particles were generally either shaped like rectangles or needles.

The diversity of shapes most likely arose from particles breaking apart. MIL-53(Al)-lt forms a very fine powder that adheres well to other surfaces, particularly moist surfaces with which it can form hydrogen bonds, but does not cohere well and so quickly breaks into smaller and smaller particles.

4.3 Immobilization of MIL-53(Al)

Immobilizing MIL-53(Al)-lt in S1813 photoresist resulted in particles of MIL-53(Al) agglomerating into large masses. Optical microscopy shown in Figure 4.16 reveals the size of these agglomerations before polishing.

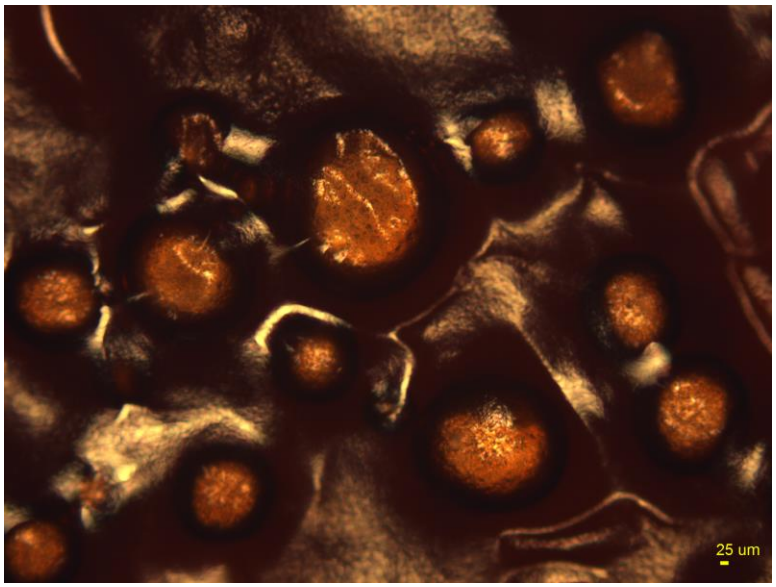

Figure 4.16: A 5x magnification optical micrograph showed large agglomerations of MIL-53(Al) particles in S1813 before polishing the sample.

XRD of the MIL-53 immobilized in S1813 reveals a change in the structure of the MIL-53(Al) as seen in Figure 4.17.

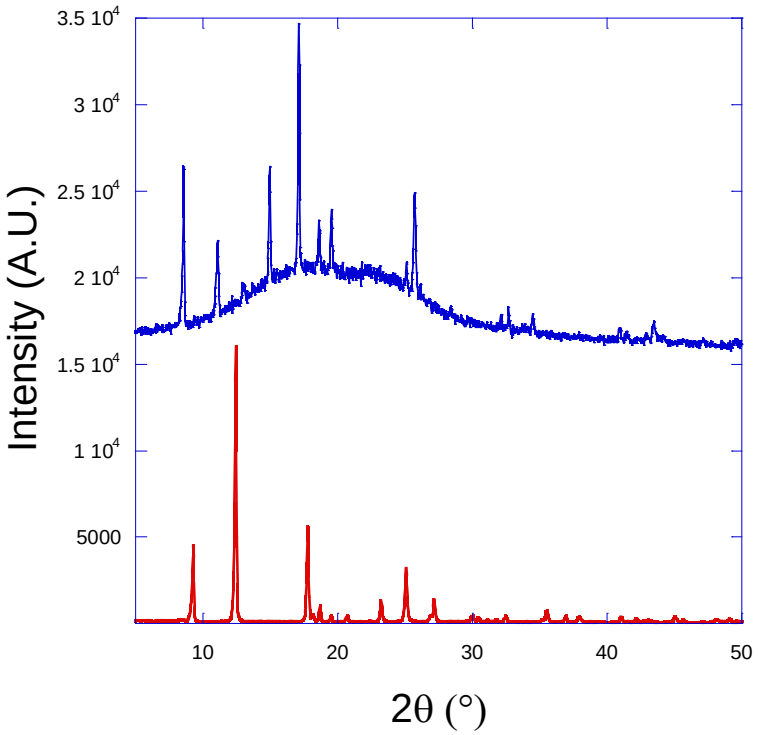

Figure 4.17: Immobilizing MIL-53 in S1813 resulted in peak shifts, changes in relative intensity of peaks, and the appearance of new peaks. The increase in background intensity came from diffraction of the amorphous S1813 photoresist.

The most likely source of the changes in the diffraction pattern is penetration of S1813 photoresist into the pores of MIL-53(Al)-lt. A different guest molecule than water occupying the pores would change the shape of the flexible MIL-53(Al) and thus the diffraction pattern.

Polishing the photoresist samples revealed densely-packed clusters of MIL-53(Al) surrounded by areas of photoresist populated with fewer MIL-53(Al) particles as shown in Figure 4.18.

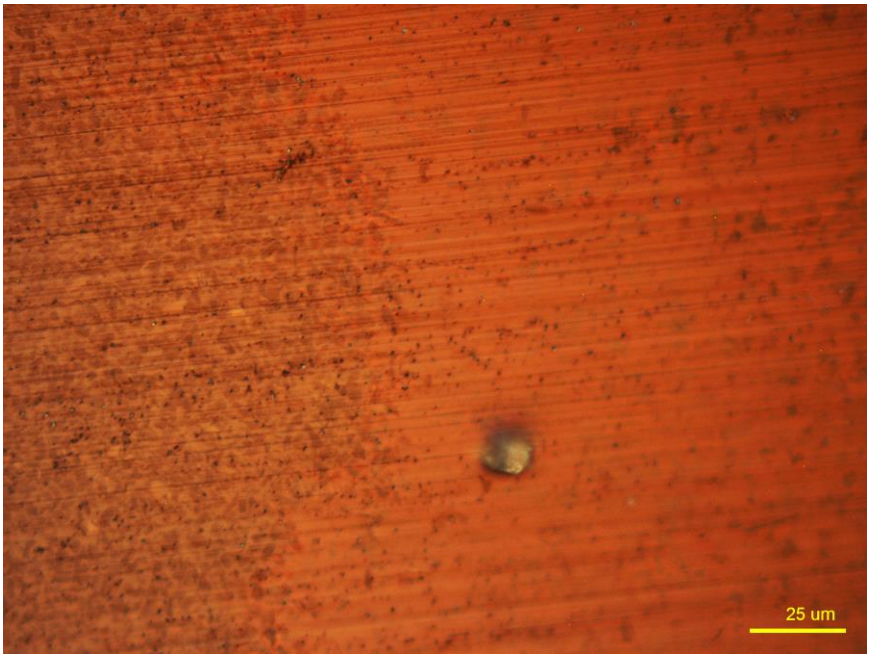

Figure 4.18: A 50x magnification optical micrograph of MIL-53 in S1813 after polishing revealed that the MIL-53 particles clustered together in the S1813 photoresist with fewer particles dispersed throughout the photoresist.

Large particles of MIL-53(Al) had broken apart inside the S1813 and moved throughout the photoresist during the process of mixing the S1813 and MIL-53(Al) to form a composite. SEM was carried out on the MIL-53 immobilized in S1813 photoresist to obtain greater magnification, shown in Figures 4.19 through 4.21.

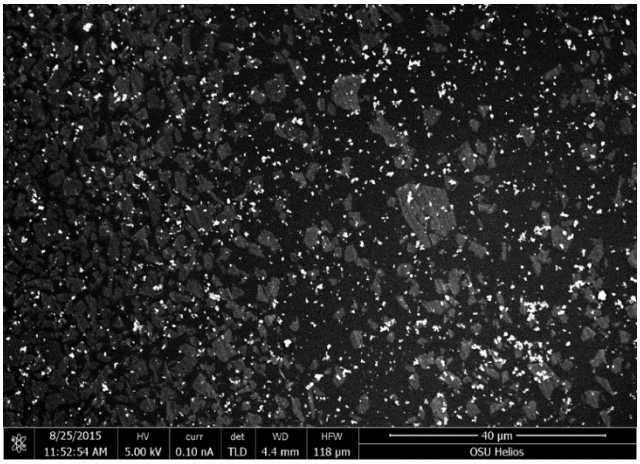

Figure 4.19: SEM imaging revealed the same clustering of MIL-53(Al) particles as optical microscopy. The particles ranged in size from 1 to 5 microns with some particles agglomerating to form a larger mass.

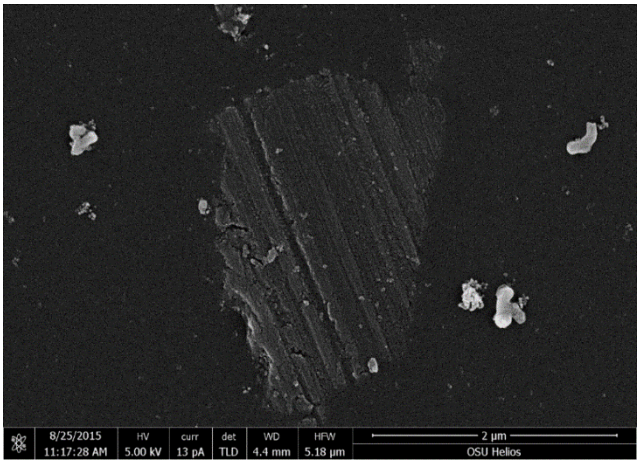

Figure 4.20: The ML-53(Al) particles showed striations all in the same direction, most likely from the polishing process.

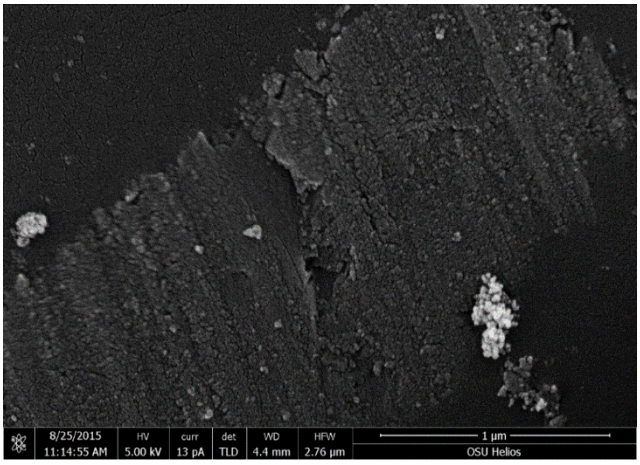

Figure 4.21: The edges of MIL-53(Al) particles were almost perfectly flush with the S1813 photoresist.

XRD was carried out on the samples after polishing. Changes in structure occur from before polishing the sample to after polishing the sample. Figure 4.22 compares the diffraction patterns of MIL-53(Al)-lt immediately after drying, MIL-53(Al) in S1813 before polishing, and MIL-53(Al) in S1813 after polishing.

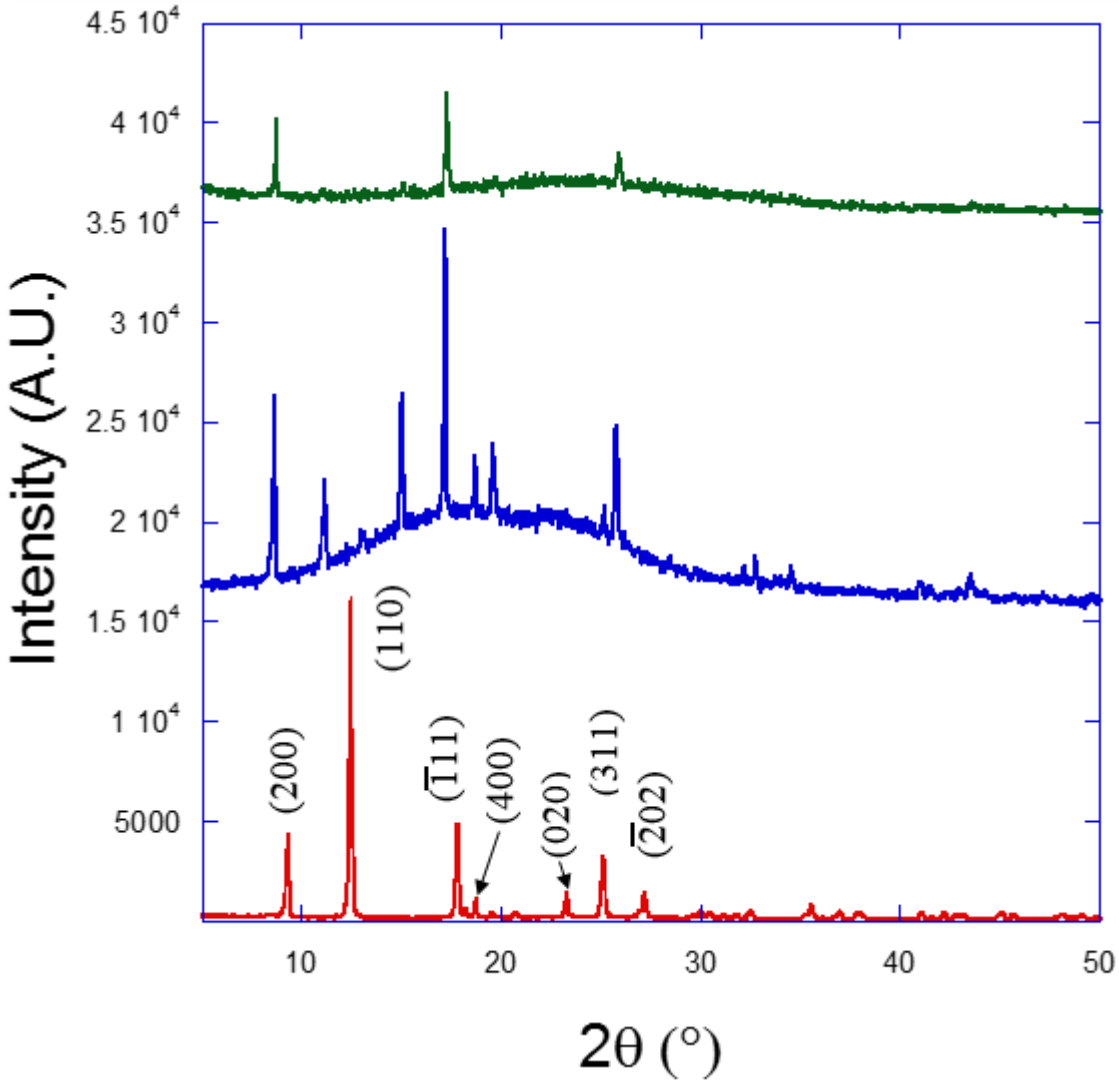

Figure 4.22: The original MIL-53(Al)-lt is shown in red, the MIL-53(Al) in S1813 before polishing in blue, and the MIL-53(Al) in S1813 after polishing in green. Polishing the MIL-53 immobilized in photoresist resulted in the disappearance of many peaks from before polishing.

Very few peaks remained after the complete polishing process. Only peaks at 8.7, 17.3, and 25.9 degrees remained after polishing MIL-53(Al) in S1813. Most likely distortions in the structure of MIL-53(Al)-lt resulted from S1813 entering the pores. These distortions would result in peak shifts. Damage and further distortions occurred as the polishing process altered the structure of MIL-53(Al) in S1813, causing many of the peaks to disappear entirely.

4.4 Nanoindentation of MIL-53(Al) in S1813

Nanoindentation was first carried out on S1813 photoresist by itself to determine its elastic modulus. The photoresist was indented in a 45 µm by 45 µm grid as seen in Figure 4.23.

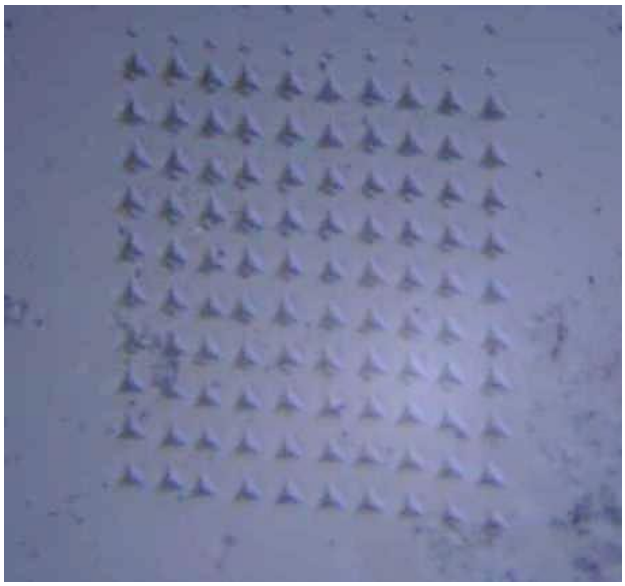

Figure 4.23: S1813 photoresist was indented 100 times in a 45 by 45 µm grid at a maximum load of 2 mN.

The resulting load-displacement curves are shown in Figure 4.24.

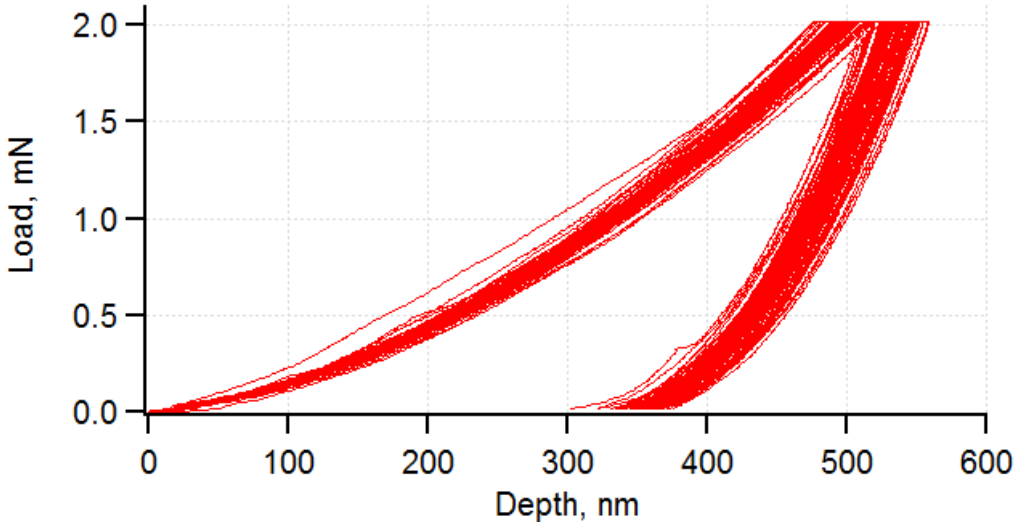

Figure 4.24: 100 indentations on S1813 photoresist resulted in fairly consistent measurements. Even before analysis of the load-displacement curves, one can see that the S1813 photoresist is isotropic from the way the load-displacement curves mostly fall on top of one another.

The load-displacement curves were analyzed using the Oliver-Pharr method to obtain elastic modulus and the results plotted in a histogram as seen in Figure 4.25.

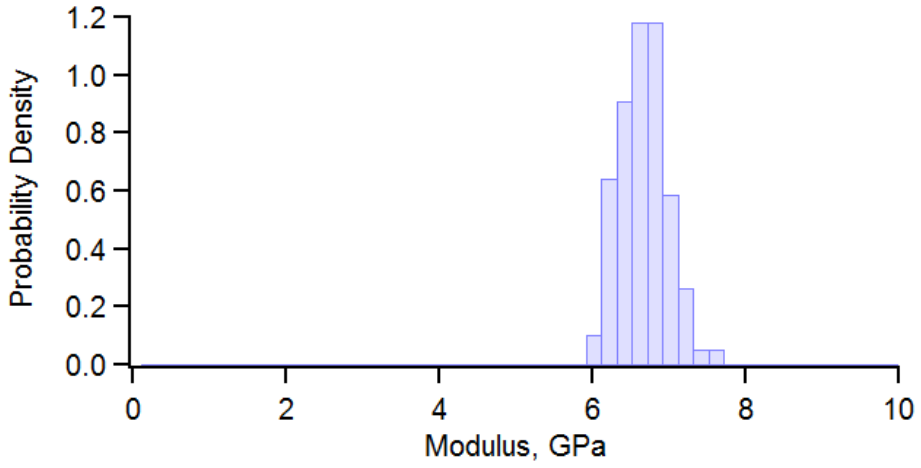

Figure 4.25: This histogram compiles the elastic moduli calculated from the load-displacement curves for S1813. The bin size is 0.2 GPa.

The elastic moduli were averaged and one standard deviation was calculated. Figure 4.26 plots each individual elastic modulus calculation along with the average and standard deviation.

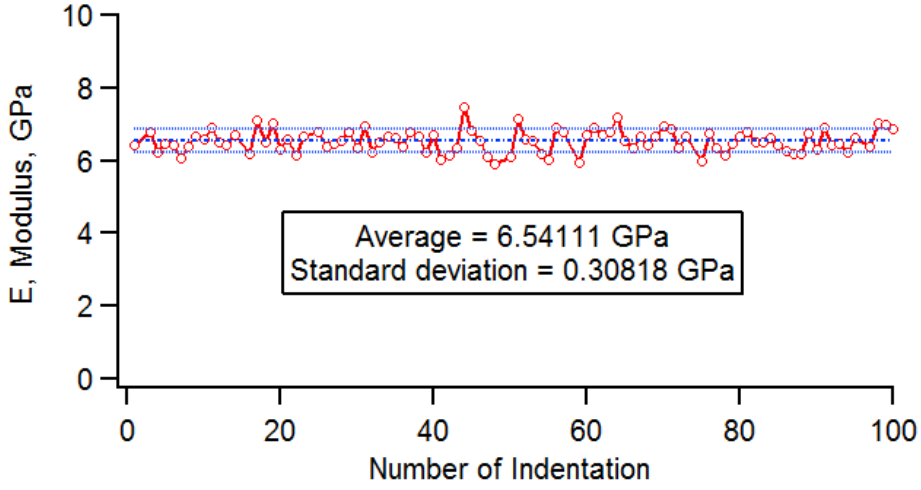

Figure 4.26: The middle blue dark blue line represents the average while the two lighter blue lines represent plus or minus one standard deviation.

The average elastic modulus of the S1813 photoresist plus or minus one standard deviation was 6.54 ± 0.308 GPa. A map of the 100 indentations and the corresponding measured elastic modulus are plotted together in Figure 4.27.

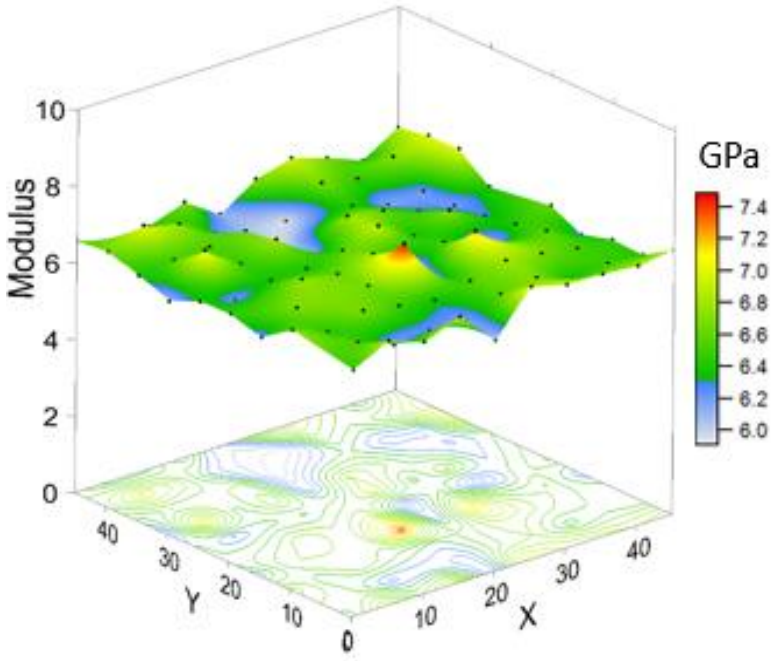

Figure 4.27: Mapping the point of each elastic modulus measurement reveals that elastic moduli values are evenly dispersed across the surface of the sample.

Overall, the nanoindentation results for the S1813 photoresist matched expectations. S1813, being an amorphous polymer, should be isotropic. There were no concentrated areas of drastically higher or lower elastic moduli.

Nanoindentation of the immobilized MIL-53(Al) was first carried out in 45 µm by 45 µm grid as seen in Figure 4.28.

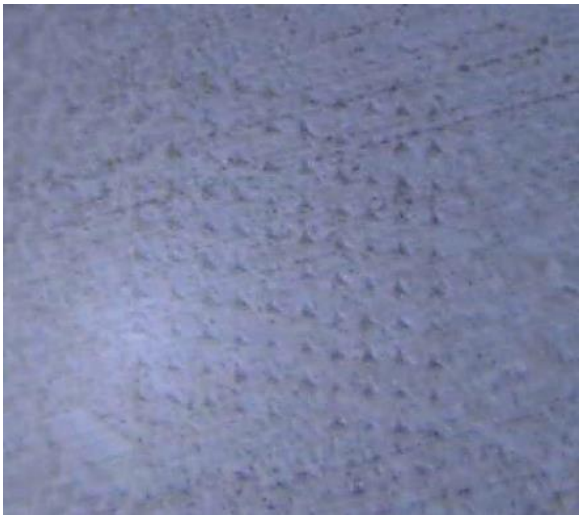

Figure 4.28: MIL-53(Al) in S1813 was indented 100 times in a 45 µm by 45 µm grid at a maximum load of 2 mN.

The resulting load-displacement curves were plotted together in Figure 4.29.

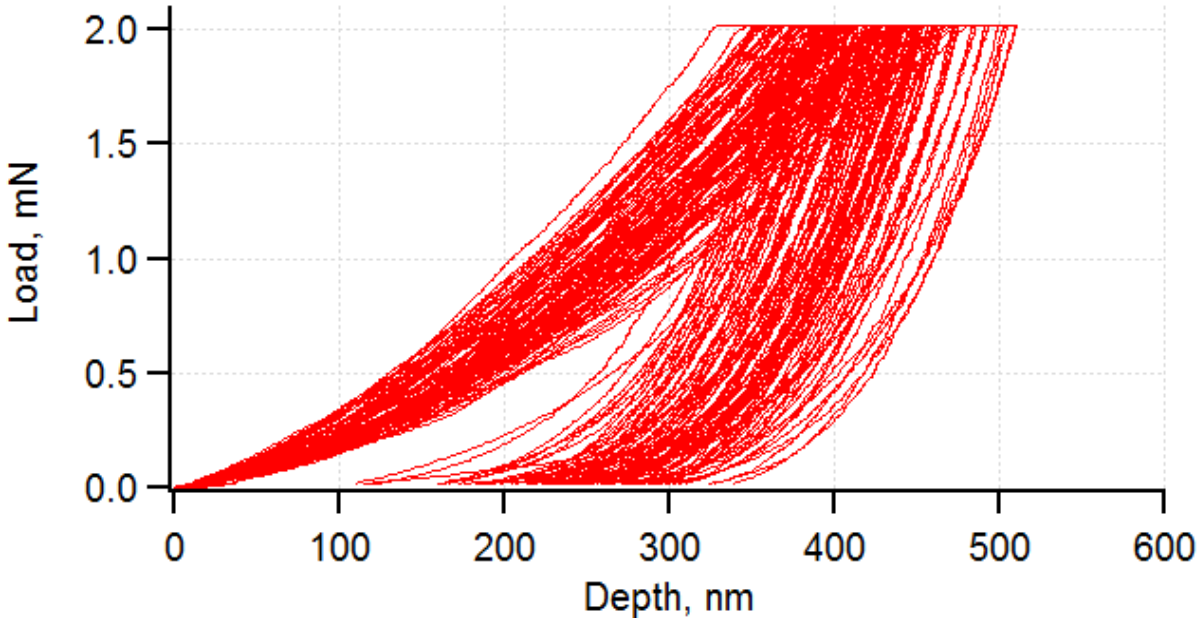

Figure 4.29: The load-displacement curves of MIL-53(Al) in S1813 were much more dispersed.

The wide spread of the load-displacement curves immediately pointed to the MIL-53 immobilized in S1813 being much more anisotropic. The elastic moduli were calculated from the load-displacement curves and plotted in a histogram to confirm this result.

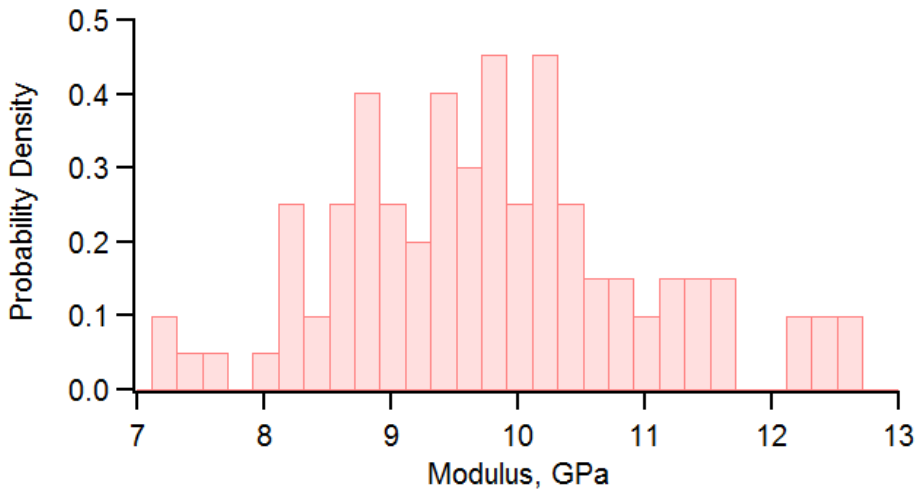

Figure 4.30: This histogram compiles the elastic moduli calculated from the indentations of MIL-53(Al) in S1813. The bin size is 0.2 GPa.

The elastic moduli were plotted point by point to better visualize the distribution of elastic moduli over the sample area.

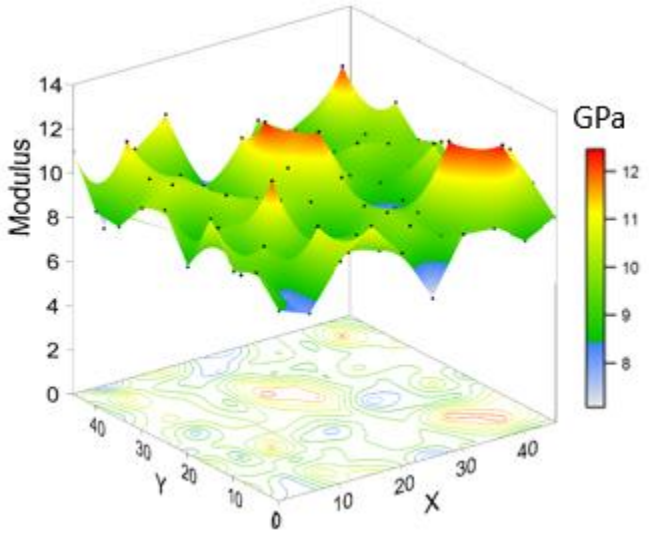

Figure 4.31: This map plots the elastic modulus calculated from each point of the indentation experiment.

The map revealed areas of higher elastic moduli surrounded by large regions of lower elastic moduli. Anisotropy was expected for MIL-53 particles, but most likely this distribution was the result of the small particle size of MIL-53. The indenter indented both MIL-53 particles and the photoresist in between MIL-53 particles, leading to matrix

effects. Thus, the calculated elastic moduli are a combination of the elastic moduli of the MIL-53 particles, the photoresist, and interaction between the two.

In order to reduce the matrix effects, lower indentation forces were chosen since lower indentation forces result in less influence from the surrounding area on the measurement. The maximum load was reduced to 1 mN and finally 0.5 mN. Figures 4.34 and 4.35 plot the 1 mN and 0.5 mN load-displacement curves, respectively.

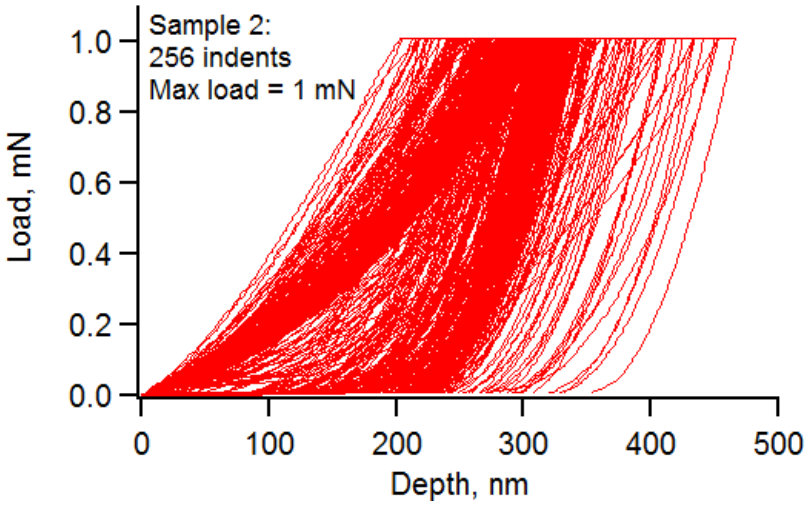

Figure 4.34: This plot shows the load-displacement measurements from the 1 mN indentations of MIL-53(Al) in S1813.

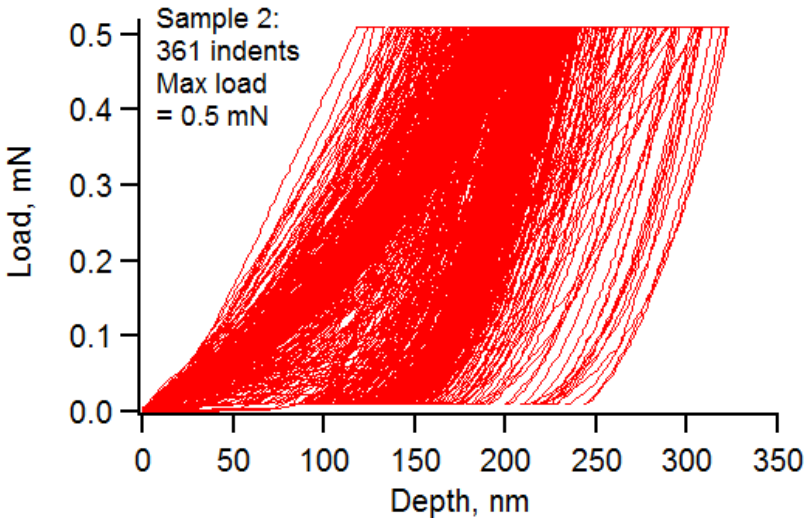

Figure 4.35: This plot shows the load-displacement measurements from the 0.5 mN indentations of MIL-53(Al) in S1813.

The elastic moduli for both the 1 mN and 0.5 mN indentations were calculated and compared with the results from the 2 mN measurements.

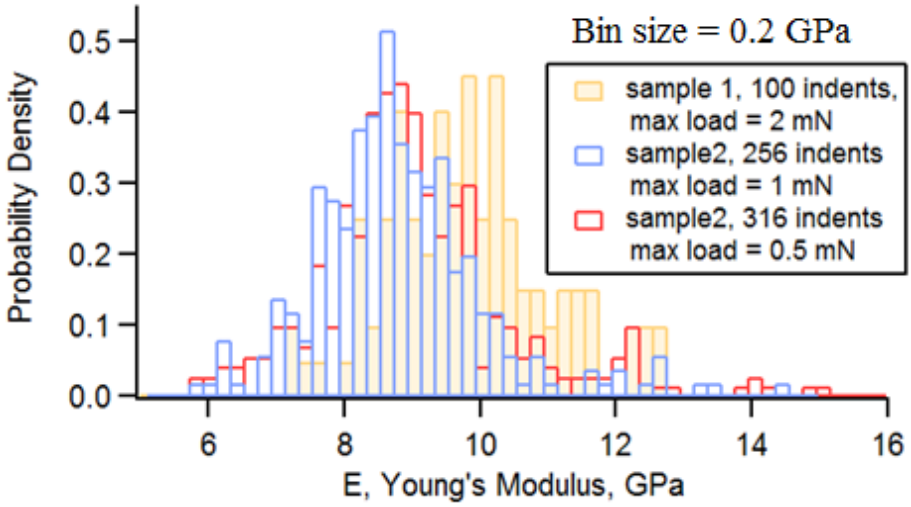

Figure 4.36: This histogram compares the calculated elastic moduli from the 2 mN, 1 mN, and 0.5 mN indentation experiments. The yellow, blue, and red bars correspond to 2 mN, 1 mN, and 0.5 mN elastic moduli calculations, respectively. The bin size is 0.2 GPa.

Reducing the indentation forces did seem to reduce the influence of matrix effects. The indentations at 1 mN and 0.5 mN resulted in a greater range of calculated elastic moduli, presumably from the indenter being influenced more by either pure MIL-53(Al) or pure photoresist. However, the matrix effects persisted, as evidenced by majority of the distributions in Figure 4.36 remaining in-between the elastic modulus of S1813 and the expected elastic modulus of MIL-53(Al). Furthermore, combining the 0.5 and 1 mN measurements in one histogram showed that the measurements still gravitated towards the elastic modulus of S1813, as seen in Figure 4.37.

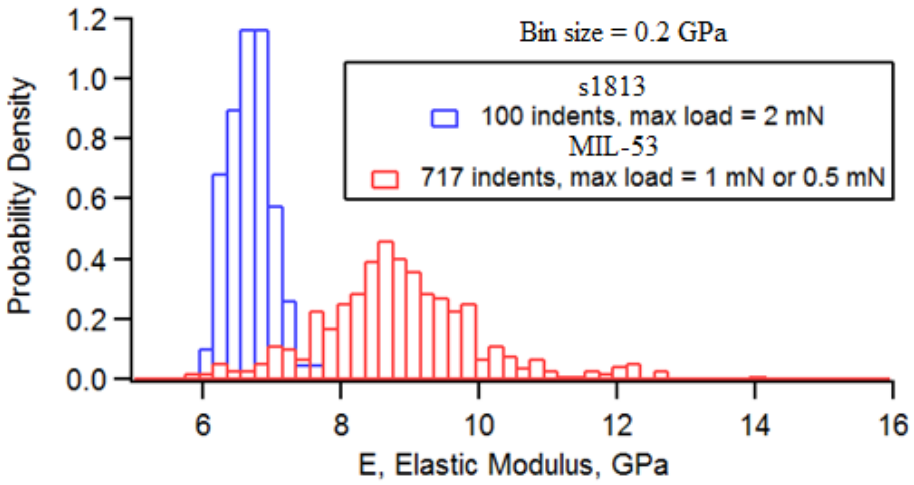

Figure 4.37: This histogram combines the elastic moduli calculated from the 1 mN and 0.5 mN indentations. The red bars are the MIL-53(Al) elastic moduli while the blue bars are the S1813 elastic moduli. The bin size is 0.2 GPa.

One source of uncertainty was assuming a Poisson's ratio of 0.3 for MIL-53(Al). The porous nature of MOFs as well as their unique structures generate many unusual properties. For example, the wine-rack structure of MIL-53(Al) leads to a negative linear compressibility in its large pore form [34]. Furthermore, framework structures like MOFs and zeolites can display auxetic properties—a negative Poisson's ratio in certain directions within the framework [35]. Therefore, an estimate of 0.3 was, in all likelihood, not very accurate. However, properties like Poisson's ratio are not very well characterized in MOFs, so empirical information on these properties was not available.

4.5 AMFM of MIL-53(Al) in S1813

AMFM was also performed on the polished samples of MIL-53(Al) in S1813. The average elastic modulus of S1813 calculated from the nanoindentation experiments provided a standard for AMFM measurements. Without measurements including at least one material of known modulus, only qualitative information, such as the ratio of elastic moduli of different materials in a scan, would be known with confidence. Any quantitative information would be an approximation. Once the modulus of the S1813 was

known, though, quantitative information could be extracted from the scans, namely the modulus of the MIL-53(Al) particles immobilized in S1813. Areas with high concentrations and low concentrations of MIL-53(Al) were scanned as seen in Figures 4.38 and 4.39.

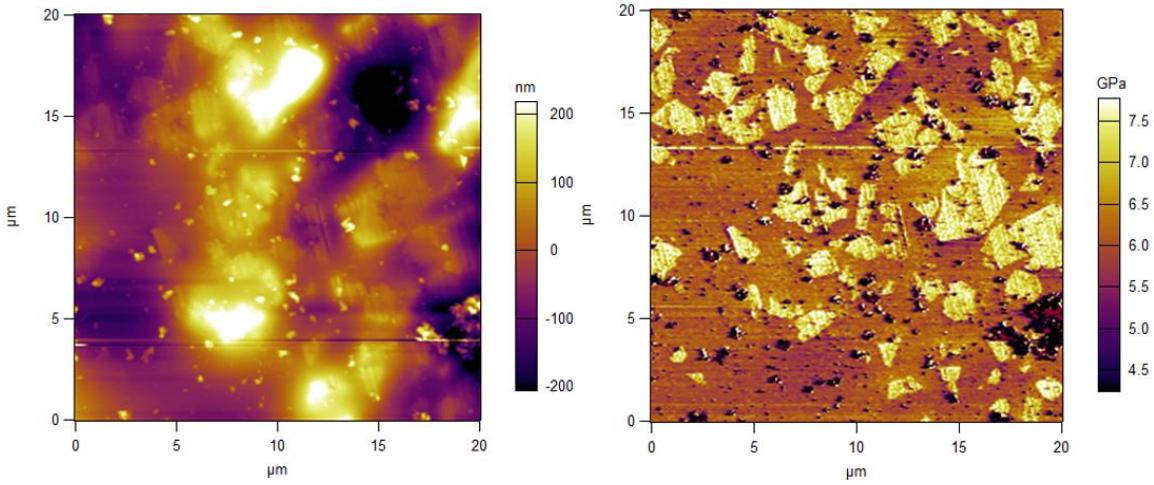

Figure 4.38: This scan area had a large concentration of MIL-53(Al) particles. The topography scan is shown on the left and the elastic modulus scan on the right.

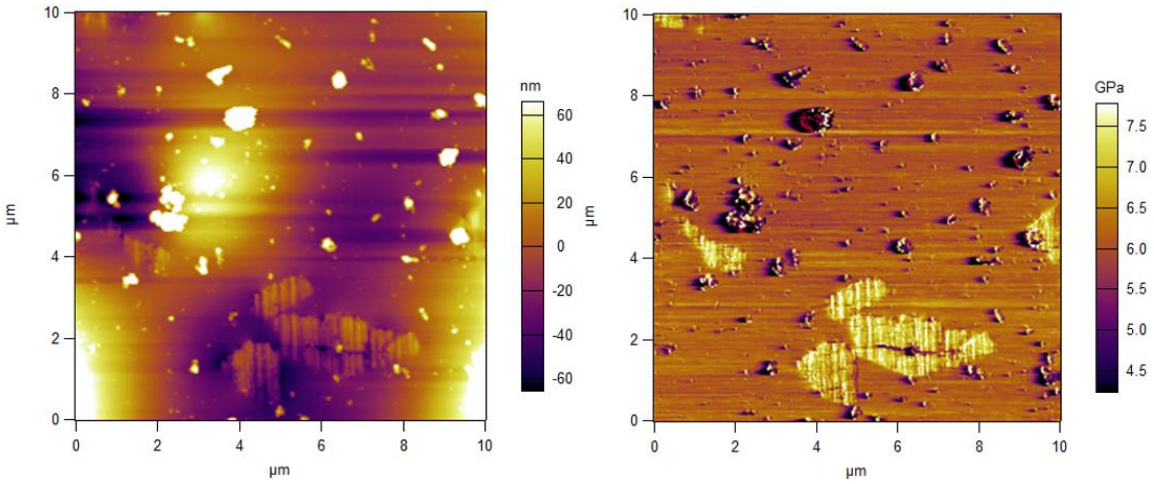

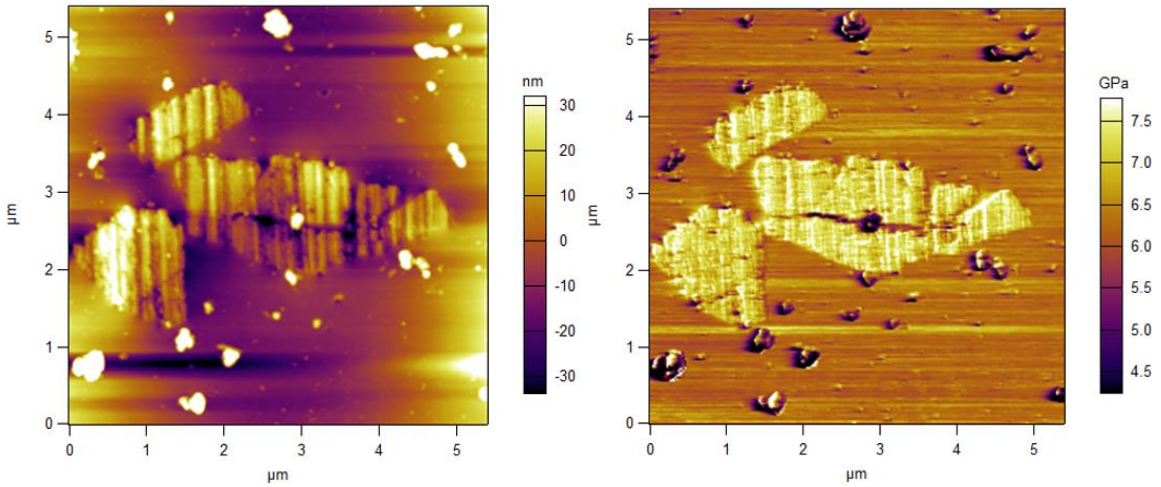

Figure 4.39: This scan area had a low concentration of MIL-53(Al) particles. The topography scan is shown on the left and the elastic modulus scan on the right.

The elastic moduli of MIL-53(Al) particles were clearly influenced both by immobilization in S1813 and the polishing process. The elastic moduli of the particles were expected to be much more anisotropic. The lack of anisotropy could have been the result of any number of factors: the change in structure of MIL-53(Al) after immobilization in S1813, the change in structure after polishing, and/or the isotropic nature of S1813. Furthermore, the small differences in elastic moduli within MIL-53(Al) particles clearly followed the striations left from polishing, as seen in the topography scans and the matching striations in the elastic moduli scans.

Another drawback of using S1813 was the inability to effectively clean the samples. Sonication destroyed the samples. Therefore, only rinsing with DI water and drying was employed, leaving the contamination seen in both the topography and elastic moduli scans. A new medium was required for immobilizing the MIL-53(Al) that was more robust.

4.6 MIL-53(Al) in Buehler Epoxy

Buehler epoxy was chosen as an alternative medium for immobilizing MIL-53(Al) in order to remove some of the disadvantages arising from immobilizing MIL-53(Al) in S1813. The immobilization process left a small portion of the surface of MIL-53(Al) agglomerations exposed as seen in Figure 4.40.

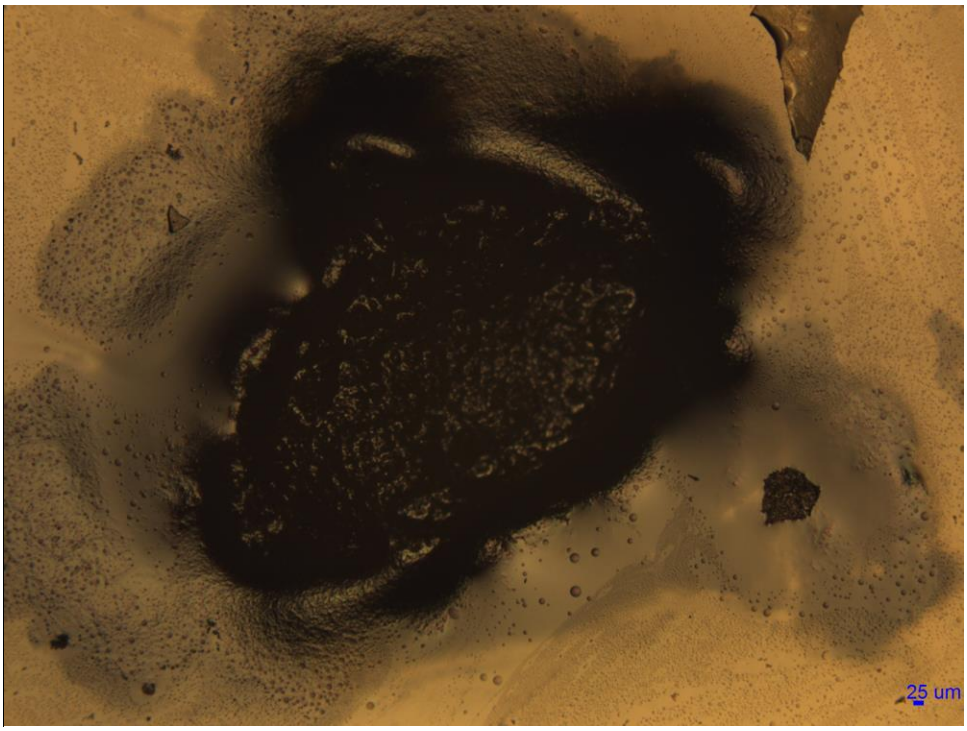

Figure 4.40: Immobilizing MIL-53(Al) in Buehler epoxy left a small portion of the MIL-53(Al) agglomerations exposed through the surface of the epoxy, as seen from optical microscopy. The magnification is 5x.

XRD of the MIL-53 immobilized in Buehler epoxy revealed that the structure of MIL-53 changed as a result of immobilization in Buehler epoxy. Both peak shifts and changes in relative intensity were evident as seen in Figure 4.41.

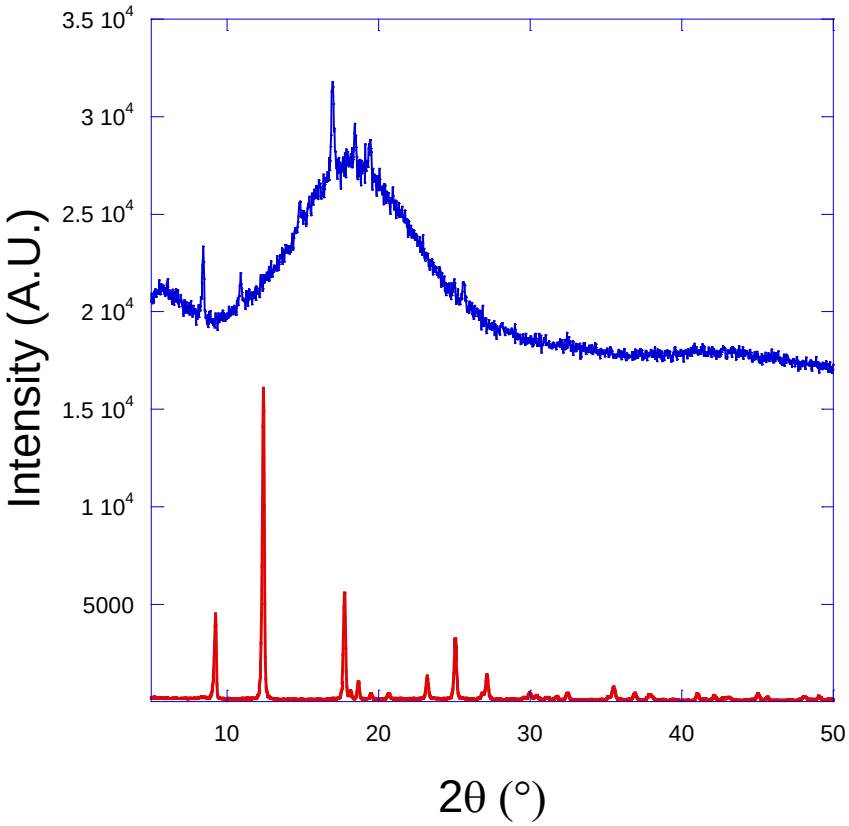

Figure 4.41: The diffraction pattern of MIL-53(Al)-lt is shown in red. The diffraction pattern of MIL-53(Al) in Buehler epoxy before polishing is shown in blue. The broad peak from 10 to 30 degrees corresponds to the Buehler epoxy.

The polishing process for MIL-53 in Buehler epoxy created a sample similar to the MIL-53 in S1813. Large clusters of MIL-53 in Buehler epoxy were surrounded areas with a much lower concentration of MIL-53 particles as seen in Figures 4.42 and 4.43.

Figure 4.42: 20x magnification revealed large clusters of MIL-53(Al) were surrounded by regions with fewer MIL-53(Al) particles.

Figure 4.43: The MIL-53(Al) particles were largely level with the surrounding Buehler epoxy. The magnification is 50x.

The polishing process affected the relative intensity of many diffraction peaks from before the polishing process. Figure 4.44 compares the diffraction patterns before and after the polishing process.

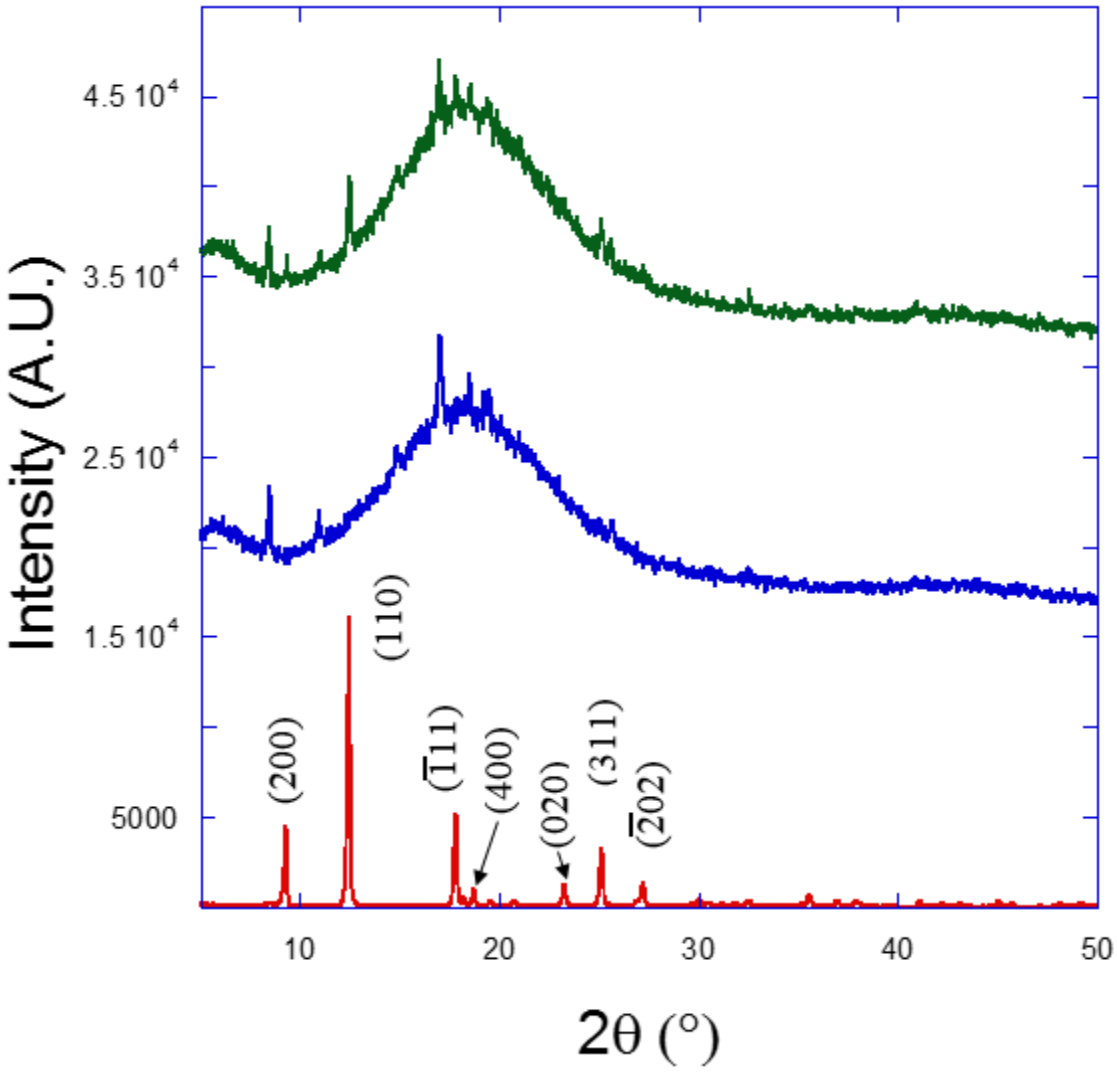

Figure 4.44: Red corresponds to the original MIL-53(Al)-lt. Blue and green correspond to MIL-53(Al) in Buehler epoxy before and after polishing, respectively. The polishing process saw a change in the relative intensity of many peaks.

The peaks of MIL-53(Al)-lt in Buehler epoxy better survived the immobilization and polishing process than MIL-53(Al)-lt in S1813. The peaks seemingly shifted after immobilization in epoxy but before polishing, which would make sense if epoxy entered the pores of MIL-53(Al)-lt and distorted the structure. In particular, the (200) and (110) appear to have shifted after immobilization in epoxy. However, many more peaks persisted for MIL-53(Al) in epoxy than in S1813.

4.7 AMFM of MIL-53(Al) in Buehler Epoxy

AMFM was carried out on the MIL-53(Al) samples in Buehler epoxy in the same manner as the samples in S1813. Nanoindentation was no longer needed for two reasons. First, the S1813 samples served as calibration samples. Therefore, so long as the same tip was used to scan epoxy samples, the scans were already known to be calibrated. Second, nanoindentation on S1813 samples had shown that the nanoindenter was not sensitive enough to consistently measure the small MIL-53(Al) particles, whereas AMFM could consistently differentiate MIL-53(Al) from the surrounding medium. Figures 4.45 and 4.46 on the next two pages show AMFM scans from regions with high and low concentrations of MIL-53(Al), respectively.

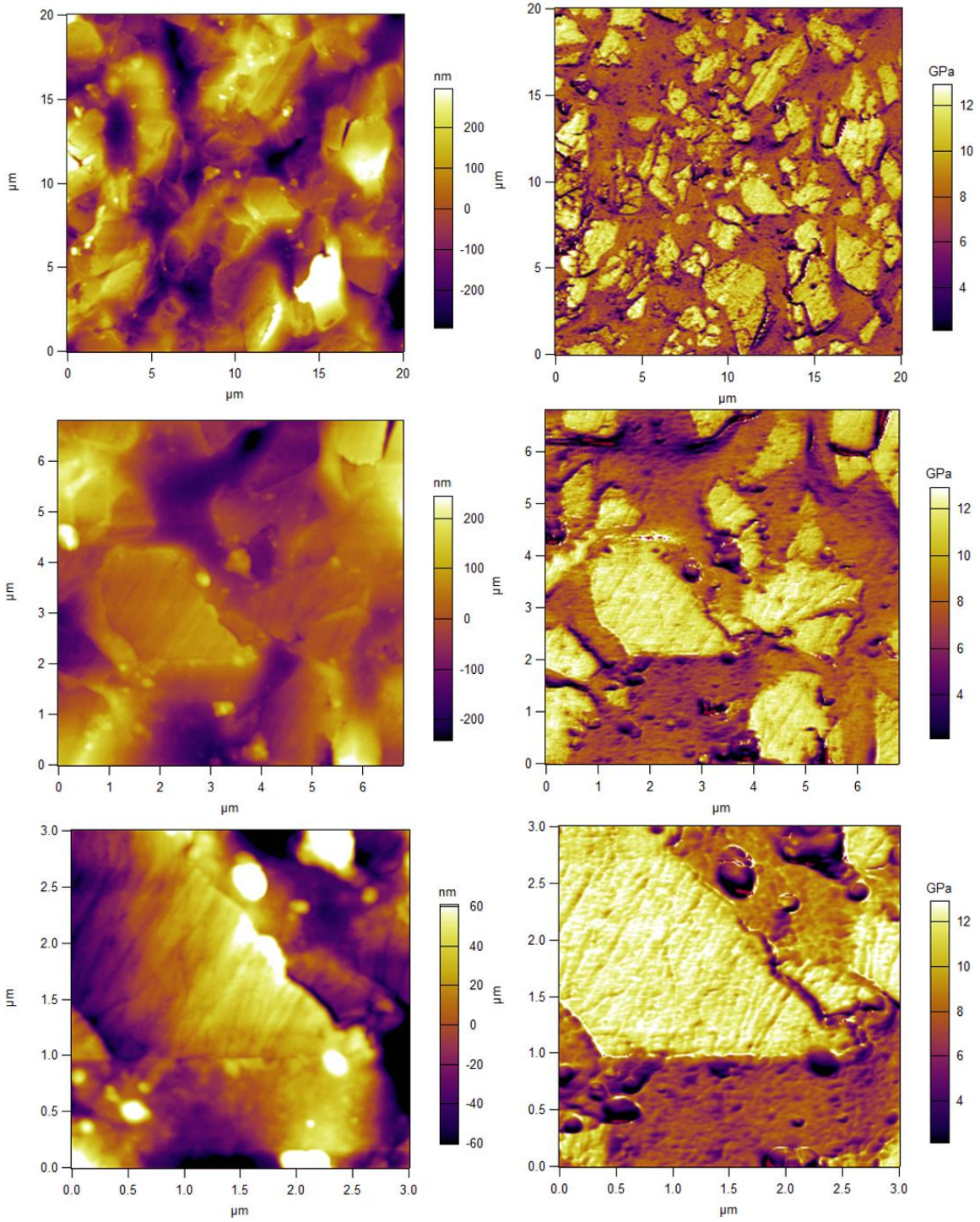

Figure 4.45: This scan area had a higher concentration of MIL-53(Al).

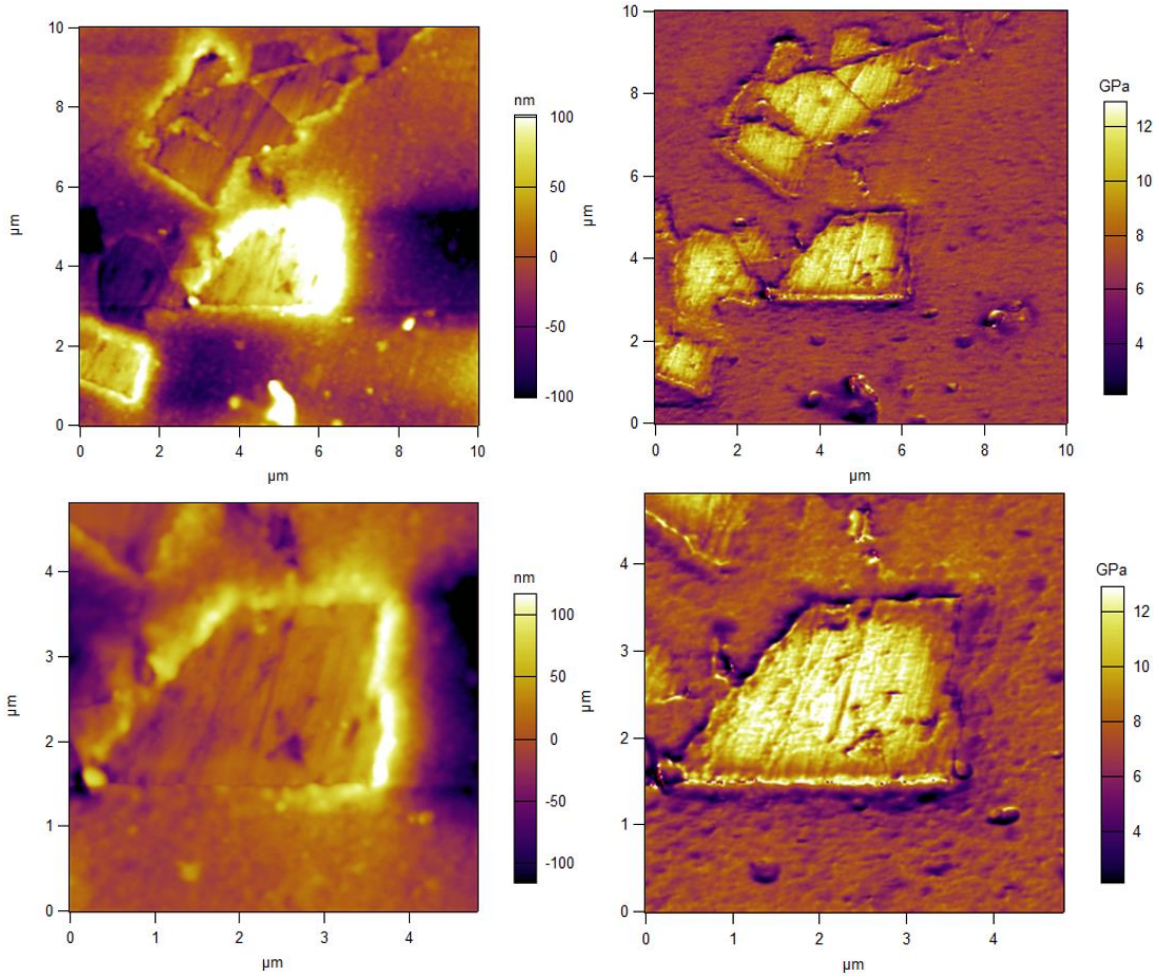

Figure 4.46: This scan area had a lower concentration of MIL-53(Al).

Once more, the medium used to immobilize MIL-53(Al) played a role in its mechanical properties. The outer regions of the MIL-53 particles show a much closer elastic modulus to the Buehler epoxy's elastic modulus. This effect was particularly pronounced in regions with low concentration of MIL-53(Al) particles. These observations strongly suggested that the epoxy matrix was influencing the elastic modulus measurements of the MIL-53 particles, especially near the edges of MIL-53(Al) particles and in regions on low MIL-53(Al) concentration.

Furthermore, the expected anisotropy of MIL-53(Al) was not seen. However, the MIL-53(Al) particles in Buehler epoxy did show greater contrast with the surrounding

medium than MIL-53(Al) particles in S1813. The Buehler epoxy was also more robust, allowing for a better cleaning process that greatly contributed to high quality AMFM scans. AMFM once more displayed a much greater capability to differentiate mechanical properties on a small scale beyond the capabilities of nanoindentation.

Chapter 5: Conclusions and Future Work

5.1 Synthesis of MOFs

Phase pure MOF-5 and MIL-53(Al) were successfully synthesized following the methods of Panella *et al.* and Loiseau *et al.*, respectively. MOF-5 required purification with DMF to obtain the desired structure, and the structure of MOF-5 quickly broke down in ambient conditions containing water vapor.

The synthesis procedure for MIL-53(Al) was altered to accommodate a larger pressure than the vessel used by Loiseau *et al.* XRD confirmed the structure of MIL-53(Al)-as before drying and MIL-53(Al)-lt after drying. Incomplete activation of MIL-53(Al)-as was detected with XRD and TGA. Optical microscopy and SEM provided images of MIL-53(Al)-lt.

5.2 Immobilization of MOFs

MIL-53(Al) was first immobilized in S1813 photoresist. XRD showed that the structure of MIL-53(Al) changed in response to being immobilized in S1813, likely from S1813 entering the pores of MIL-53(Al). The MIL-53(Al) in S1813 samples were polished, and XRD again detected a change in structure in response to polishing. Optical microscopy and SEM after polishing showed large clusters of MIL-53(Al) with particles ranging in size from 1 to 5 μm.

MIL-53 was also immobilized in Buehler epoxy. XRD showed that the structure changed after being immobilized in epoxy. The structure also changed after polishing with many changes in the relative intensity of peaks. Optical microscopy revealed that MIL-53(Al) in Buehler epoxy looked much like MIL-53(Al) in S1813, with dense

clusters of MIL-53(Al) surrounded by more sparse areas of Buehler epoxy and MIL-53(Al).

5.3 Mechanical Characterization of MOFs

Nanoindentation of S1813 by itself determined that the photoresist was isotropic with an average elastic modulus plus or minus one standard deviation of 6.54 ± 0.308 GPa. Nanoindentation of MIL-53(Al) in S1813 displayed a much more anisotropic response. The source of the response could have come from a number of sources. MIL-53(Al) was expected to be anisotropic based on theoretical calculations. However, mapping the calculated moduli on a map of the sample revealed that the apparent anisotropy was more likely a result of matrix effects from indenting both MIL-53(Al) and S1813. Lowering the indentation forces reduced the effects of the matrix but did not remove them.

AMFM of MIL-53(Al) in S1813 generated images with MIL-53(Al) distinguishable from the surrounding photoresist matrix. Furthermore, the nanoindentation results allowed for calibration of the AMFM scans since the value of the elastic modulus of S1813 was already known as well as the isotropy of S1813. However, the expected anisotropy of the MIL-53(Al) did not appear. Furthermore, the effects of the polishing process could be seen from comparing the topography and elastic modulus scans. The combination of immobilization and polishing clearly affected the MIL-53(Al) samples in S1813.

AMFM of MIL-53(Al) in Buehler epoxy generated more promising results. The contrast in elastic modulus between the MIL-53(Al) and Buehler epoxy was much clearer than in S1813. Furthermore, the greater robustness of the epoxy allowed for a better

cleaning process, resulting in higher quality images. However, the expected anisotropy of MIL-53(Al) was once more not observed. The scans also revealed the effect of the Buehler epoxy matrix on the MIL-53(Al). The centers of MIL-53(Al) particles had a higher elastic modulus than edge regions of the particles. This results most likely arose from the diminishing effect of the epoxy matrix the farther the scans got from the epoxy matrix into the center of MIL-53(Al) particles.

5.4 Future Work

Clearly a method to produce suitably flat MOF surfaces without the effects from immobilization or polishing is needed. New mediums could be explored that are less likely to affect the structure of the MOFs wanting to be characterized. Alternatively, MOFs more amendable to characterization by nanoindentation and AMFM without alteration could be synthesized.

More nanoindentation needs to be done in order to understand the matrix effects associated with immobilizing MOFs. More intimate knowledge of these effects would allow for better extraction of useful mechanical information from nanoindentation and AMFM experiments. Furthermore, the quantitative information gathered from AMFM could be used more extensively. The AFM software provides spreadsheets of the data used to generate the images from AMFM. This data could be employed in theoretical work with MOFs either to generate new models or corroborate already existing models.

The long-term hope is to provide as much information as possible for use with theoretical models. The empirical information generated by mechanical characterization of MOFs allows for refinement of models calculating the various properties of MOFs. As these models get better, they can then guide synthesis of MOFs with particular properties

in mind. These models also provide the potential for designing new MOFs. Theoretical MOFs could be constructed from a repository of known node and linkers and tested for their properties. This way the most efficient use of resources can be achieved for tackling the astronomically large design space surrounding MOFs and their properties.

Bibliography

[1] J.R. Li, J. Sculley, H.C. Zhou. Chemical Reviews. 112 (2012) 869–932.

[2] C. Janiak, J.K. Vieth. New Journal of Chemistry. 34 (2010) 2366.

[3] S. Horike, S. Shimomura, S. Kitagawa. Nature Chemistry. 1 (2009) 695–704.

[4] G. Férey. Chem. Soc. Rev. 37 (2008) 191–214.

[5] S.T. Meek, J.A. Greathouse, M.D. Allendorf. Advanced Materials. 23 (2011) 249–267.

[6] R.J. Kuppler, D.J. Timmons, Q.-R. Fang, J.R. Li, T.A. Makal, M.D. Young, D. Yuan, D. Zhao, W. Zhuang, H.C. Zhou. Coordination Chemistry Reviews. 253 (2009) 3042–3066.

[7] O.K. Farha, J.T. Hupp. Accounts of Chemical Research. 43 (2010) 1166–1175.

[8] N. Stock, S. Biswas. Chemical Reviews. 112 (2012) 933–969.

[9] A.K. Cheetham, C.N.R. Rao, R.K. Feller. Chemical Communications. (2006) 4780.

[10] H. Li, M. Eddaoudi, M. O'Keeffe, O. M. Yaghi. Nature. 402 (1999) 276-279.

[11] O.M. Yaghi, M. O'Keeffe, N.W. Ockwig, H.K. Chae, M. Eddaoudi, J. Kim. Nature. 423 (2003) 705–714.

[12] B. Panella, M. Hirscher. Advanced Materials. 17 (2005) 538–541.

[13] G. Férey, C. Serre, Chemical Society Reviews 38 (2009) 1380.

[14] S. Kitagawa, R. Kitaura, S. Noro. Angewandte Chemie International Edition. 43 (2004) 2334–2375.

[15] A. Schneemann, V. Bon, I. Schwedler, I. Senkovska, S. Kaskel, R.A. Fischer, Chem. Soc. Rev. 43 (2014) 6062–6096.

[16] T. Loiseau, C. Serre, C. Huguenard, G. Fink, F. Taulelle, M. Henry, T. Bataille, G. Férey. Chemistry - A European Journal. 10 (2004) 1373–1382.

[17] J.C. Tan, A.K. Cheetham. Chemical Society Reviews. 40 (2011) 1059.

[18] W. Li, S. Henke, A.K. Cheetham. APL Materials. 2 (2014) 123902.

[19] A. Gouldstone, N. Chollacoop, M. Dao, J. Li, A. Minor, Y. Shen. Acta Materialia. 55 (2007) 4015–4039.

[20] "How to Select the Correct Indenter Tip." Agilent Technologies. Accessed 28 October 2015.

[21] W.C. Oliver, G.M. Pharr. J. Mater. Res. 7 (1992) 1564-1583.

[22] D.F. Bahr, J.A. Reid, W.M. Mook, C.A. Bauer, R. Stumpf, A.J. Skulan, N.R. Moody, B.A. Simmons, M.M. Shindel, M.D. Allendorf. Physical Review B. 76 (2007).

[23] J.J. Vlassak, W.D. Nix. J. Mech. Phys. Solids. 42 (1994) 1223-1245.

[24] A.U. Ortiz, A. Boutin, A.H. Fuchs, F.-X. Coudert. The Journal of Chemical Physics. 138 (2013) 174703.

[25] Peter Eaton and Paul West. *Atomic Force Microscopy.* Oxford University Press. 2010.

[26] Ryan Fuierer. "Procedural Operation 'Manualette.'" Asylum Research. 2009.

[27] "MFP-3D Manual." Asylum Research. 2008.

[28] H.J. Butt, B. Cappella, M. Kappl. Surface Science Reports. 59 (2005) 1–152.

[29] G. Haugstad. "On 'non-contact' and 'tapping mode' AFM." 2011.

[30] D. Hurley, M. Kocun, I. Revenko, B. Ohler, R. Proksch. "Fast, quantitative AFM nanomechanical measurements using AM-FM Viscoelastic Mapping Mode." Microscopy and Analysis. March/April 2015.

[31] R. Garcia, R. Proksch. European Polymer Journal. 49 (2013) 1897–1906.

[32] "AM-FM Viscoelastic Mapping Mode." Asylum Research.

[33] T. Limpoco, M. Kocun, W. Meinhold, A. Labuda, R. Proksch. "Quantitative Elastic Measurements of High Modulus Materials with Tapping/AM-FM Mode." Advanced Materials Characterization Workshop. June 2015.

[34] P. Serra-Crespo, A. Dikhtiarenko, E. Stavitski, J. Juan-Alcañiz, F. Kapteijn, F.X. Coudert, J. Gascon. Cryst. Eng. Comm. 17 (2015) 276-280.

[35] F.X. Coudert. Chem. Mater. 27 (2015) 1905-1916.